Article

Geological, Mineralogical and Geochemical Study of the Aquamarine-Bearing Yamrang Pegmatite, Eastern Nepal with Implications for Exploration Targeting

Sushmita Bhandari [1,2,3], Kezhang Qin [1,2,*], Qifeng Zhou [4] and Noreen J. Evans [5]

1   Key Laboratory of Mineral Resources, Institute of Geology and Geophysics, Chinese Academy of Sciences, Beijing 100029, China; sushgeo12@hotmail.com
2   College of Earth and Planetary Sciences, University of Chinese Academy of Sciences, Beijing 100049, China
3   Department of Mines and Geology, Ministry of Industry Commerce and Supplies, Government of Nepal, Kathmandu 44600, Nepal
4   Institute of Mineral Resources Research, China Metallurgical Geology Bureau, Beijing 101300, China; zhouqifeng85@163.com
5   School of Earth and Planetary Sciences, John de Laeter Centre, Curtin University, Perth, WA 6845, Australia; noreen.evans@curtin.edu.au
*   Correspondence: kzq@mail.iggcas.ac.cn

Abstract: The Yamrang Pegmatite in the Ikhabu Pegmatite Field, Eastern Nepal is Nepal's primary source of aquamarine. This paper reports detailed mineralogy and whole rock granite and pegmatite geochemistry, and major and trace element data for alkali feldspar and muscovite in order to classify the aquamarine-bearing Yamrang Pegmatite, elucidate beryl-saturation processes and evaluate potential geochemical exploration tools for beryl-pegmatites. Five internal mineralogical/textural zones were identified in the Yamrang Pegmatite; zone 1 (saccharoidal albite); zone 2 (blocky perthitic microcline); zone 3 (muscovite–microcline–quartz); zone 4 (beryl-quartz), and zone 5 (miarolitic cavities). Zones 1–4 represent the magmatic stage, while zone 5 formed during the hydrothermal stage of pegmatite genesis. Spectacular aquamarines are recovered from miarolitic zone 5, while beryl saturation is found in zones 3, 4, and 5. Based on beryllium (Be) content, Be partition among co-existing minerals at the magmatic stage is beryl > muscovite > tourmaline > alkali feldspar > quartz. In contrast, the sequence at the hydrothermal stage is beryl > muscovite > albite > tourmaline > quartz. The Be content in rock-forming minerals decreases from pegmatite margin to core, and tourmaline could have played a significant role in Be enrichment processes in the marginal pegmatite zone. High temperature, a low degree of fractionation, and the dominance of Be-compatible mineral phases such as muscovite, calcium-rich alkali feldspar and tourmaline resulted in beryl undersaturation in marginal zones. However, low temperature, high fractional crystallization, and low abundance of Be-compatible mineral phases resulted in beryl saturation in inner zones. The strongly peraluminous nature, low total REE content (<500 ppm), mineral assemblage of beryl, tourmaline, spessartine, columbite-tantalite, depletion of Ba, Nb, and enrichment of Pb, Rb, Cs in the primitive mantle normalized multi-element plots suggest that the beryl-bearing Yamrang Pegmatite corresponds to the LCT pegmatite family. Alkali feldspar with K/Rb values of 30–150, Rb ~3000 ppm, Cs >100 ppm, and muscovite, with K/Rb ranging 18–50, Rb ~6000 ppm, Cs > 500 ppm, and Ta > 65 ppm in inner zones (3–5), indicate that the Yamrang Pegmatite is an intermediate-fractionated, beryl-type rare-element (REL) pegmatite. It is probable that whole rock Be content of >10 ppm could be considered an exploration guide to beryl mineralization in the region.

1. Introduction

Beryl ($Be_3Al_2Si_6O_{18}$) is an important beryllium (Be) ore and a valuable gem. It is the most common Be mineral in the Earth's crust, occurring in granites, pegmatites, and veins at magmatic and hydrothermal stages. Emerald and aquamarine are the most valuable gem varieties of beryl, formed by the addition of chromophores Cr^{3+}/V^{3+} for green emerald and Fe^{3+} for blue aquamarine. Rare-element pegmatites (REL) are a major source of beryl and other rare metals. Accounting for 1–2% of all granitic pegmatites, they may contain significant amounts of beryl, lithium aluminosilicates, phosphates, except for apatite, oxides, except for magnetite or ilmenite, and other rare minerals [1]. The study and classification of pegmatites primarily focuses on their rare-element mineralogy with REL pegmatites widely classified into the LCT (enriched in Li, Cs, Ta) or NYF (enriched in Nb, Y, F) petrogenetic families [2,3]. LCT pegmatites are of great economic interest as they host several economic rare-metal minerals such as spodumene, lepidolite, pollucite, petalite, columbite-tantalite, beryl, cassiterite, etc. Besides being an important Be ore and valuable gem, beryl is an early rare-metal mineral, crystallizing from fertile magma, that may evolve to deposit Nb, Ta, Li, Cs minerals. Hence, establishing the geological, geochemical, and mineralogical characteristics of beryl pegmatite has ramifications for the exploration of other highly economic commodities.

We investigated the field geology, mineralogy, and whole rock chemistry of pegmatites and granites from Eastern Nepal in order to identify barren and Be-rich bodies. We then concentrated our detailed studies on beryl-mineralized pegmatites in the Ikhabu Pegmatite Field (IPF), focusing on the large Yamrang Pegmatite. The Yamrang Pegmatite is intruded on the lower part of the Higher Himalayan Sequence in the Taplejung district of Eastern Nepal (Figure 1).

For the first time, this study reports major and trace element data for alkali feldspar and muscovite from the Yamrang Pegmatite, and whole rock chemistry of barren and Be-rich pegmatites from the region. The Be partition sequence in rock-forming minerals is compared with experimental data. This contribution aims to classify the beryl-bearing pegmatites from the area, investigate the beryl-saturation process and evaluate potential geochemical exploration guides for beryl-pegmatites. Results will provide the first insights into the properties of REL pegmatites from the region and aid in rare-metal exploration in the Himalayan belt in general, and in similar tectonic settings elsewhere.

2. Regional Geological Setting

2.1. Geology

The Himalayan orogenic belt resulted from the Cenozoic Indo-Asian collision along the Yarlung–Zangbo Suture Zone and extends 2400 km from Namche Barwa in the east to Nanga Parbat in the west. It comprises the Sub-Himalayan sequence, Lesser Himalayan sequence (LHS), Higher Himalayan sequence (HHS), and Tethyan Himalayan sequence (THS) from south to north (Figure 1).

The Eastern Nepal Higher Himalaya (Tamor–Kanchenjunga region) is bounded by the Main Central Thrust (MCT) in the south and South Tibetan Detachment System (STDS) in the north, and is divided into three lithological units; (a) Junbesi Paragneiss, (b) Kanchenjunga Migmatite, and (c) Kanchenjunga Paragneiss (Sil-Bt quartzo-feldspathic paragneiss in Figure 1) formation from the bottom to top [4–6]. They are correlated with Formation I, II, and III of Le Fort (1975) [7], respectively.

The Precambrian to Cambrian Junbesi Paragneiss (Formation I) is a 4–7 km thick unit with St-Ky gneiss at the lower part and Sil-grade migmatitic gneiss, concordant leucosomes, and discrete leucogranite dikes and sills at the top [4–6] (Figure 1). The gradational boundary between Junbesi Paragneiss and Kanchenjunga Migmatite (Formation II) is marked by an increased proportion of Sil-migmatite and roughly coincides with the position of the High Himal Thrust (HHT 1) [4,8]. The Kanchenjunga Migmatite is a 5–18 km thick unit comprising a sillimanite ± cordierite-bearing migmatitic gneiss, and quartzite with subordinate calc-

silicates metabasites [6]. Cordierite-bearing migmatites appear in the mid-portion of the Kanchenjunga Migmatite and are restricted to the north of HHT 2 [8,9] (Figure 1).
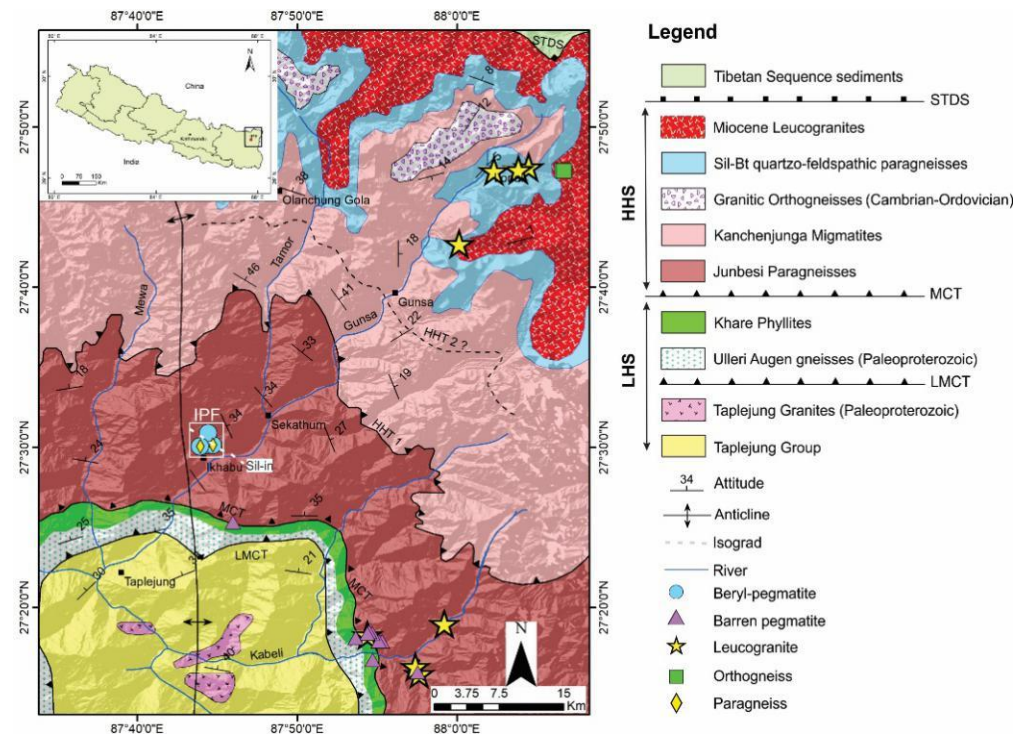
Figure 1. Regional Geological Map of Tamor–Kanchenjunga region, Eastern Nepal, showing the Ikhabu Pegmatite Field (IPF) and sample locations (compiled after [4–6,8]. Lower data clusters show the Chyanthapu area, and upper data clusters show the Kanchenjunga area. Abbreviations: LHS, Lesser Himalayan Sequence; HHS, Higher Himalayan Sequence; LMCT, Lower Main Central Thrust; MCT, Main Central Thrust; HHT, High Himal Thrust (HHT-1, HHT of [4]; HHT-2, HHT of [5]); STDS, South Tibet Detachment System; Bt, biotite; Sil, sillimanite. Mineral abbreviations are after [10].

The Kangchenjunga Migmatite has a gradational boundary with the overlying Kanchenjunga Paragneiss (Formation III) (Schelling, 1992). The Kanchenjunga Paragneiss formation is a 3–6 km thick unit consisting of Bt-Sil-gneiss/schist, quartzite, and widespread intrusions of Cambrian–Ordovician granites (510–480 Ma, now orthogneiss) [7,11–13] and Miocene (23–12 Ma) leucogranite sills and dikes [14–16] (Figures 1 and 2a–d).

Figure 2. *Cont.*

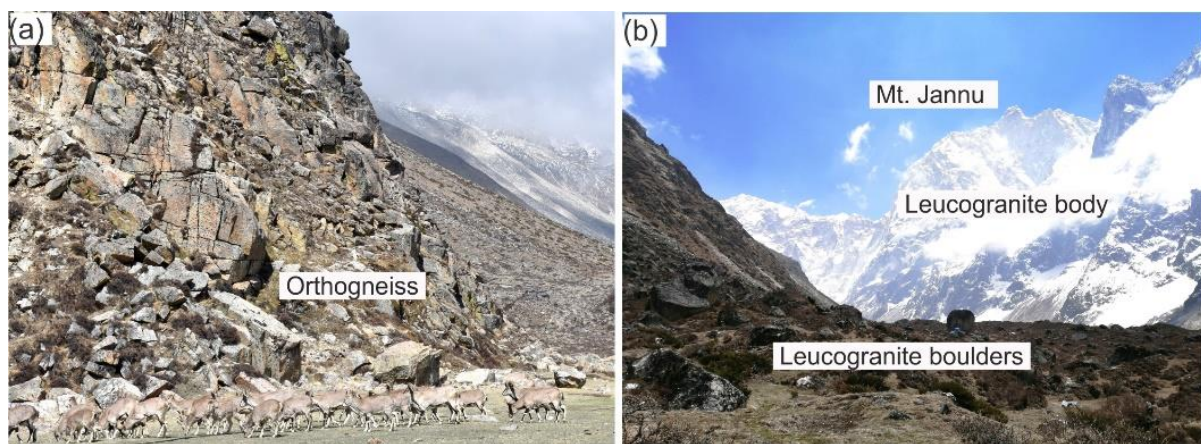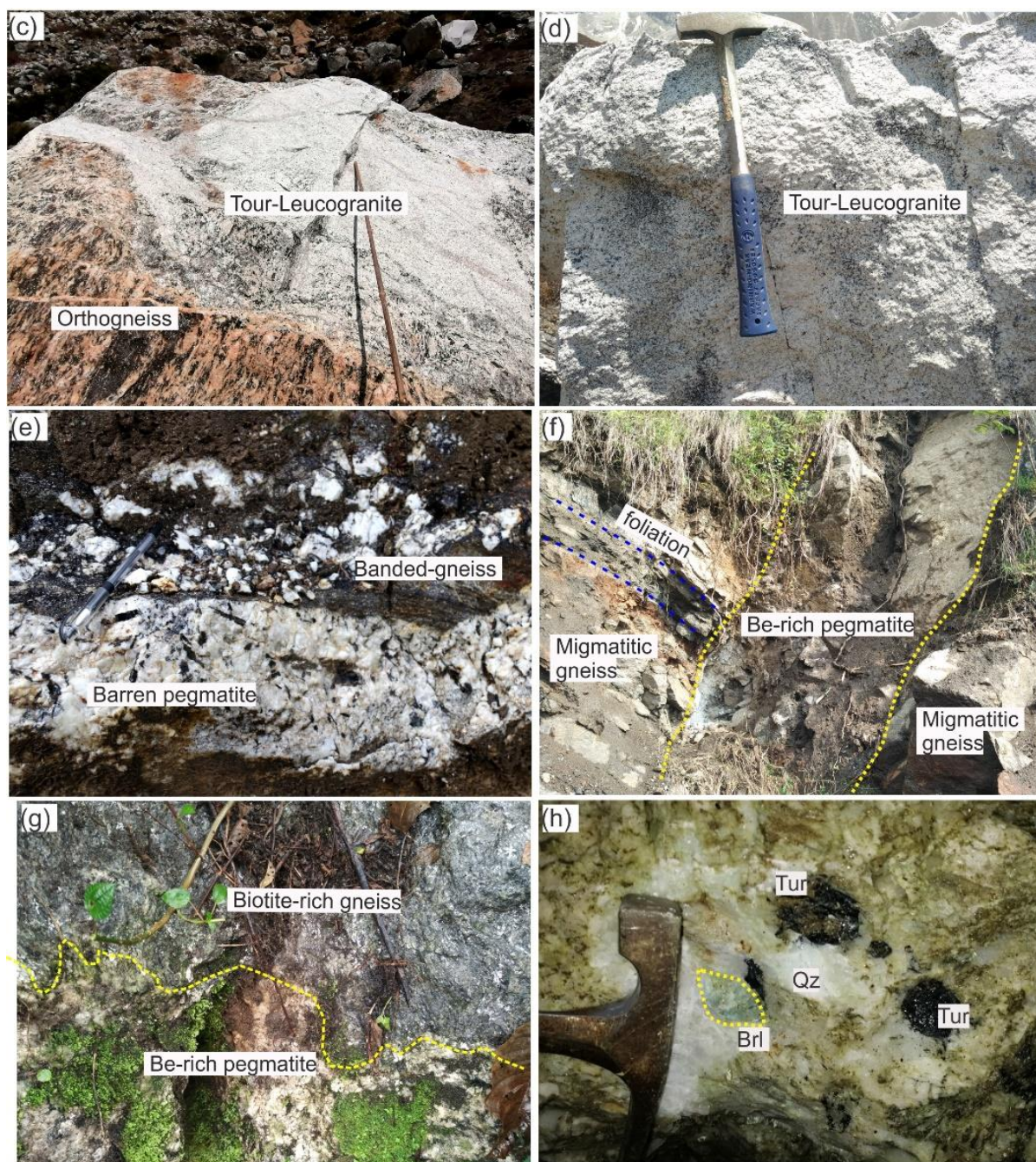**Figure 2.** Field photographs of pegmatites and granites. (**a**) Orthogneiss exposure at Lonak (Kanchenjunga area); (**b**) Field view of Kanchenjunga–Jannu leucogranite at Mt. Jannu base camp; (**c**) Tour-leucogranite crosscutting the orthogneiss; (**d**) Tour-leucogranite; (**e**) Barren pegmatite intruded on banded gneiss at Chyanthapu area; (**f**,**g**) Be-rich pegmatite showing angular and sharp contact with host-rock gneiss at Ikhabu area; (**h**) Beryl seen in the outcrop of Be-rich pegmatite at Ikhabu area. Mineral abbreviations: Brl, beryl; Qz, quartz; Tur, tourmaline. Mineral abbreviations are after [10].

The studied beryl-mineralized pegmatites belong to the Ikhabu Pegmatite Field of Eastern Nepal. They are intruded into the middle part of the Junbesi Paragneiss in the vicinity of the sillimanite-in isograd (Figure 1). The beryl pegmatites are characterized by a mineral assemblage of quartz, K-feldspar, albite, muscovite, tourmaline, garnet, beryl, and ± rutile or columbite-tantalite (Figure 2h). The host rock (kyanite to sillimanite grade, locally migmatitic gneiss; Figure 2f,g) strikes NW–SE and dips NE at 25°–35°. The studied barren pegmatites are from the lower part of the Junbesi Paragneiss, closer to the Main

Central Thrust at the Ankhop–Chyanthapu area. These pegmatites vary from 10 cm to 7 m in thickness. These are common pegmatites with a mineral assemblage of quartz, K-feldspar, albite, biotite, muscovite, tourmaline, and garnet (Figure 2e).

2.2. Granitic Plutons

Two types of granitic plutons are identified in the Eastern Nepal Higher Himalayan Sequence: (1) pre-Himalayan granites (orthogneiss) (510–480 Ma) of Kanchenjunga Paragneiss (formation III) formed by Cambrian–Ordovician magmatism [7,11–13] and (2) Himalayan leucogranites (23–12 Ma) formed by Miocene magmatism [14–16]. Leucogranites are essentially seen above HHT 1 as thin dykes and sills. The proportion of leucogranites increases from 10 to 20% at 4000 m to >60% above 6000 m altitude and they comprise the Kanchenjunga and Jannu mountain peaks [4,17]. The leucogranites at the Mt. Kanchenjunga-Mt Jannu area are known as the Kanchenjunga–Jannu leucogranites [17]. The plutons studied in this work are from the Kanchenjunga Paragneiss formation, upper part of HHS around the Lonak–Kanchenjunga–Jannu area, about 35–40 km northeast of the IPF, and from the Junbesi Paragneiss formation, lower part of HHS around Chyanthapu, about 35–40 km southeast from IPF (Figures 1 and 2).

The coarse-grained orthogneiss consists of quartz, augen-shaped K-feldspar, plagioclase, garnet, tourmaline, biotite, muscovite, and occasionally cordierite and sillimanite (Figure 2a,c). The foliation is defined by biotite, tourmaline, and augen feldspar. The leucogranite sills and dikes were intruded into paragneiss and orthogneiss (Figure 2b,c). Himalayan leucogranites are divided into four types; biotite-, two-mica (Ms > Bt)-, tourmaline-, and garnet-leucogranites, based on dominant mineralogy [18–22]. Fine to medium-grained tourmaline-leucogranite consisting of quartz, feldspar, muscovite and tourmaline is dominant in the Kanchenjunga–Jannu area (Figure 2d); however, garnet-leucogranite fragments were also found around the base camp at Mt. Kanchenjunga and Mt. Jannu. All orthogneiss samples were collected from the Kanchenjunga area, while leucogranite samples were from the Kanchenjunga–Jannu and Chyanthapu areas.

3. Geology of Yamrang Pegmatite

Aquamarines were first discovered in Nepal in 1934 [23] and they are now famous worldwide. The Ikhabu pegmatites had been previously mentioned as a source of aquamarine in Nepal [24–26]; however, no further information is available in the literature. The present work represents the first detailed geological information on the beryl (aquamarine)-bearing pegmatites from Nepal Himalaya.

The beryl-bearing Ikhabu pegmatites are intruded into Ky-Sil grade biotite-schist to migmatitic gneiss in the middle part of the Junbesi paragneiss formation (Figures 2 and 3). They are tabular to lenticular dikes with an undifferentiated, homogeneous to well-zoned character, ranging in width from 1 to 27 m and with a visible length from a few meters to 130 m. They show angular and sharp contact with country rocks (Figure 2f,g) and exhibit little to no deformation, implying that they are younger than Himalayan metamorphism. The long axes of larger dikes frequently follow the strike of the foliation, with pinched and inflated edges. The major minerals are quartz, alkali feldspar, muscovite >> biotite, with tourmaline and garnet as common accessories. Rare-metal minerals include beryl, columbite–tantalite, rutile, zircon, monazite, and xenotime (Figures 3 and 4). Big granitic bodies were not exposed in the area; however, migmatites and thin to thick leucogranite sills are frequent in the upper part of the Junbesi Paragneiss [4,5,8].
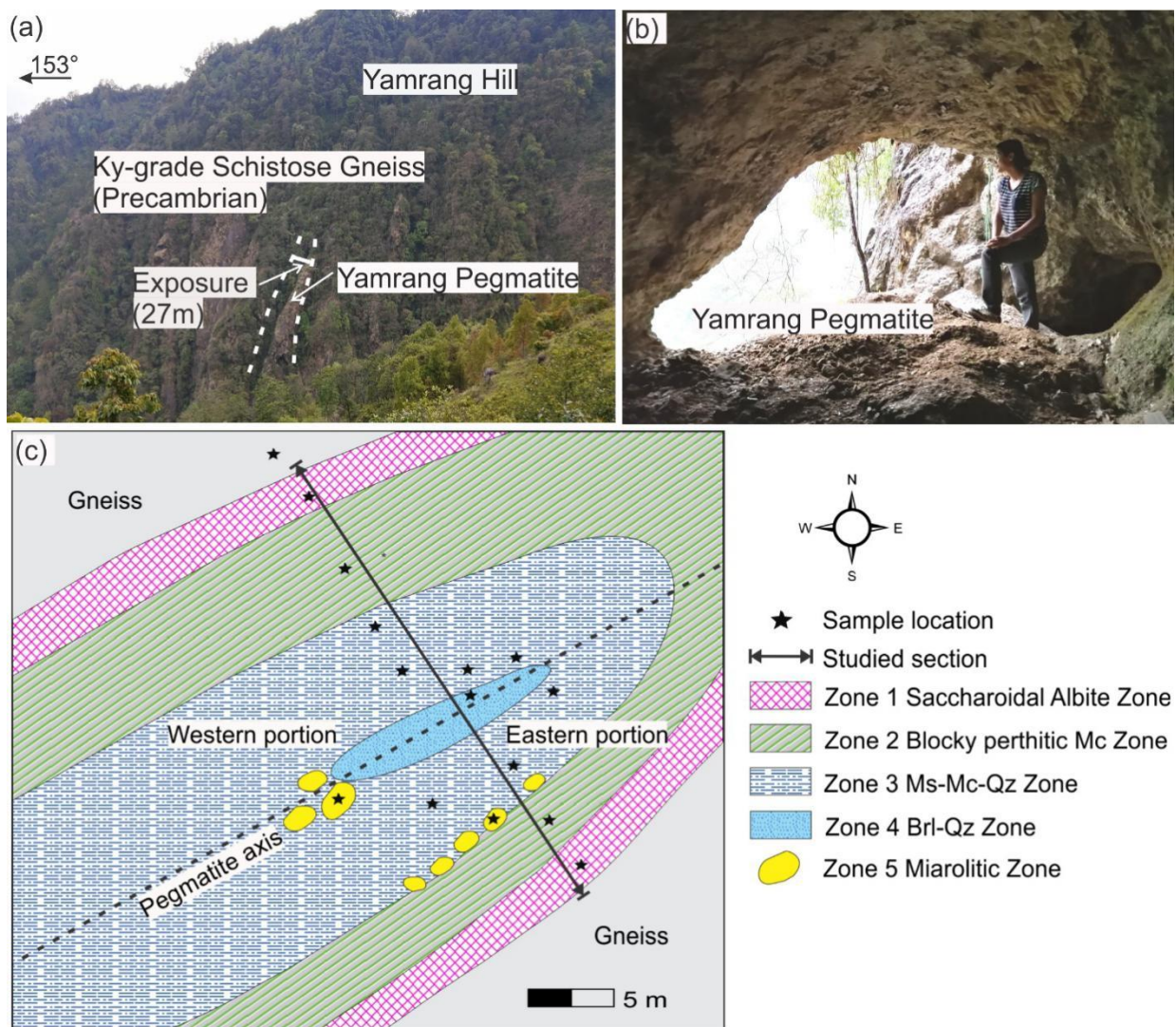
Figure 3. Field photographs and sketch map of the Yamrang Pegmatite. (**a**) Location of Yamrang Pegmatite at Yamrang hill; (**b**) Exposure of Yamrang Pegmatite, zone 3; (**c**) Schematic sketch of internal zonation of the Yamrang Pegmatite. Mineral abbreviations: Brl, beryl; Mc, microcline; Ms, muscovite; Qz, quartz. Mineral abbreviations are after [10].
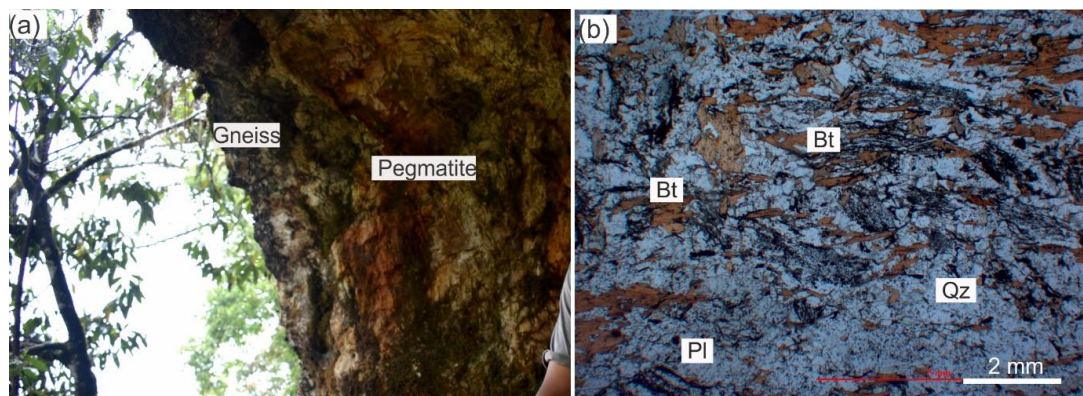

Figure 4. *Cont.*
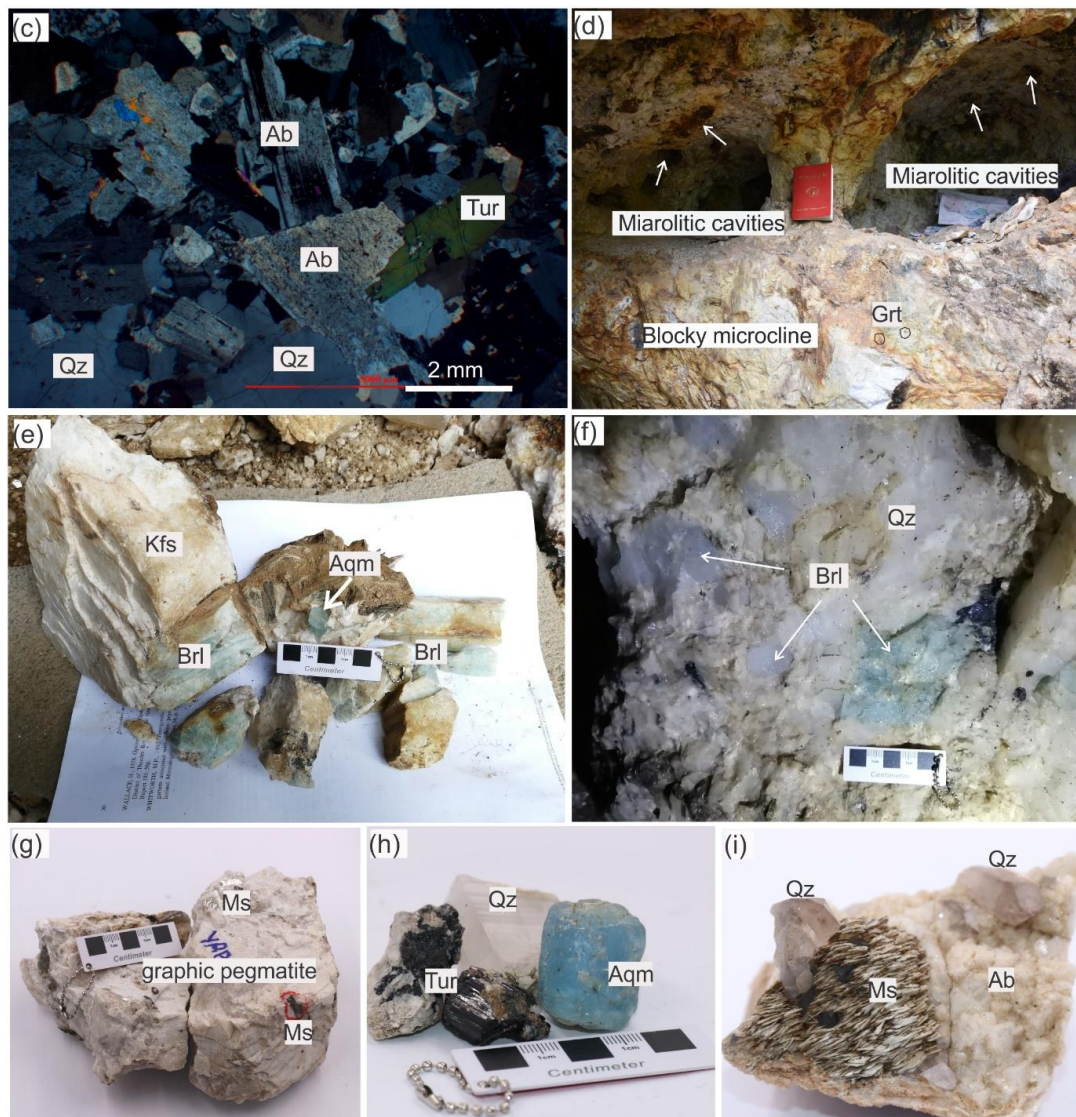
Figure 4. Field photographs and photomicrographs of the Yamrang Pegmatite. (**a**) Yamrang Pegmatite and host-rock gneiss contact zone; (**b**) Biotite-rich schistose gneiss hosting Yamrang Pegmatite under plane-polarized light; (**c**) Sample from saccharoidal albite zone showing albite-quartz assemblage; (**d**) Blocky perthitic microcline zone with miarolitic cavities; (**e**) Beryl and aquamarine in association with K-feldspar; (**f**) Quartz-beryl association from core zone; (**g**) Pegmatite sample showing graphic texture; (**h**) Aquamarine, quartz, and tourmaline gems from Yamrang Pegmatite; (**i**) Smoky quartz, muscovite books and albite assemblage from miarolitic cavities. Mineral abbreviations: Ab, albite; Aqm, aquamarine; Brl, beryl; Bt, biotite; Grt, garnet; Kfs, K-feldspar; Ms, muscovite; Pl, plagioclase; Qz, quartz; Tur, tourmaline. Mineral abbreviations are after [10].

The large Yamrang Pegmatite is located at the NE aspect of Yamrang hill at Sangsabu village in the Taplejung district, Eastern Nepal (Figure 3). The hill is steep and covered with dense vegetation. The Yamrang Pegmatite-host rock contact was not exposed in the field, however, a small section of sharp contact was observed in the roof of the Yamrang Pegmatite manual mining site. The pegmatite intruded kyanite grade, medium-grained, highly deformed, strongly foliated, biotite-rich schistose gneiss and was exposed at 1840 m elevation. Its exposed dimension is 27 m wide and 130 m long (Figure 3). The Yamrang Pegmatite shows axial-symmetric zonation and can be differentiated into five mineralogical–textural zones (Figures 3c and 4, Table 1). All zones have gradational contact except zone 5, which is overprinted on zones 2 and 3. Zones 1–4 represent the magmatic stage of the Yamrang Pegmatite, while zone 5 represents the hydrothermal stage.

Table 1. Description of internal zonation of Yamrang Pegmatite, Ikhabu Pegmatite Field (IPF), Eastern Nepal.

Zone Number	Zone Name (Sequential)	Zone Name (Mineralogical)	Thickness	Main Mineral Assemblage (Relative Abundances wt.%)	Accessory and (Rare) Minerals	Descriptive Features	Texture
Zone 1	Marginal Zone	Saccharoidal albite	2 m	Ab (56), Mc (8), Qz (30), Ms (4)	Drv-Srl, (Fl, Zrn, Mnz)	saccharoidal albite, inwardly oriented tourmaline layers	Fine to medium-grained
Zone 2	Outer Intermediate Zone	Blocky perthitic microcline	4–7 m	Ab (10), Mc (70), Qz (15), Ms (3)	Sps, Srl-Drv, (Zrn, Mnz)	Massive microcline, graphic pegmatite, platy albite, quartz lenses, muscovite clusters	monomineralic, massive
Zone 3	Inner Intermediate Zone	Muscovite-microcline-quartz	5–6 m	Ab (15), Mc (40), Qz (25), Ms (15)	Brl, Sps, Rt, Srl, (Col-Tan, Zrn, Mnz, Xtm)	coarse graphic pegmatite, platy albite, book muscovite veins, quartz-beryl pods, quartz-muscovite nests	coarse-grained to massive
Zone 4	Core Zone	Beryl-quartz	1–1.5 m	Mc (5), Qz (60), Ms (1), Brl (33)	Srl, (Zrn, Mnz)	quartz-beryl 90%, microcline patches at core margin	medium to coarse-grained
Zone 5	Miarolitic Zone	Albite-quartz	few to tens of cm	Ab (40), Mc (15), Qz (25), Ms (15)	Brl, Aqm, Col-Tan, Rt, Srl, Hem, (Zrn, Mnz, Xtm)	clay filled pockets, platy albite, dipyramidal smoky quartz, aquamarine, muscovite books, overprinted on zone 2 and 3,	fine to coarse-grained

Note: Ab, albite; Aqm, aquamarine; Mc, microcline; Qz, quartz; Ms, muscovite; Brl; beryl; Col-Tan, columbite-tantalite; Drv-Srl, dravite-schorl; Fl, fluorite; Zrn, zircon; Mnz, monazite; Sps, spessartine; Rt, rutile; Xtm, xenotime; Hem, hematite. Mineral abbreviations are after [10].

Zone 1 is the marginal saccharoidal albite zone, with a 1.5–2 m thick saccharoidal albite and quartz mineral assemblage, containing subordinate muscovite and accessory fine tourmaline (Figures 3c and 4c). Zone 2 is the blocky perthitic microcline zone, 4.5–7 m thick with a mineral assemblage of perthitic microcline + quartz ± platy albite with accessory garnet and tourmaline (Figure 4d). Zone 3 is the muscovite–microcline-quartz zone, 5–6 m thick and containing coarse perthitic-microcline, quartz, albite, muscovite, subordinate tourmaline and garnet, and rare mineral beryl, columbite-tantalite, and rutile (Figure 3b). Zone 4 is the core zone, measuring 1–1.5 m wide and consisting of a coarse beryl–quartz assemblage (Figure 4f). Zone 5 comprises a group of miarolitic cavities over-printed on zones 2 and 3, mainly along the eastern boundaries of zones 2 and 3, and 3 and 4 (Figures 3c and 4d). Aquamarine, translucent white beryls associated with platy albite, euhedral smoky quartz, book muscovite, and fine-grained columbite-tantalite are found in the miarolitic cavities (Figure 4h,i).

4. Analytical Methods

Petrographic observation and visual determination of modal mineral abundance in the thin section were performed under a polarizing microscope. Based on petrographic observation, representative samples were carefully selected for further analysis. Thin sections were used for electron probe microanalysis (EPMA), major element determination and in-situ laser ablation inductively coupled plasma mass spectrometry (LA-ICP-MS) trace element analysis of minerals.

4.1. Whole-Rock Major and Trace Element Analysis

We divided our whole rock samples into five clusters: beryl-bearing pegmatite (Ikhabu pegmatites), paragneiss (host rock of Ikhabu pegmatites), barren pegmatite, orthogneiss, and leucogranite. Fresh whole rock samples (11 beryl pegmatites, 10 barren pegmatites, 3 orthogneiss and 9 leucogranites) were selected for whole rock major and trace element analyses (Supplementary Table S1). Studying pegmatite geochemistry from representative bulk samples is challenging given the heterogeneous texture and large mineral crystals. However, when samples are chosen carefully and combined with mineral chemistry, we can still enhance our understanding of pegmatite chemistry. In the case of the zoned Yamrang Pegmatite, large samples (2–5 kg) from internal zones (zone 1-YRP-1, YRP-11, YRP-13; zone 2-YRP-2; zone 3-YRP-6, YRP-7, YRP-9; zone 5-IW-8) were selected, each representative of the texture and mineral assemblage/mineral distribution of that zone. Similarly, from the barren pegmatites and beryl-bearing Wairung (IW-1) and Sangsabu (IW-5, IW-6) pegmatites that lack internal zonation and contain giant crystals, large samples (2–5 kg) representative of texture and pegmatite mineral assemblage were selected.

Analyses were conducted at Beijing Createch Testing Technology Co. Ltd. The whole rock was crushed to 200 mesh using a tungsten carbide ball mill. Major element compositions were determined on fused glass disks using an X-ray fluorescence spectrometer (XRF-1800, SHIMADZU, Kyoto, Japan) with an analytical precision within ±2% for the oxides present in an abundance > 0.5 wt.% and within ±5% for oxides > 0.1 wt.%. Loss on ignition (LOI) was measured for each sample after heating to 1000 °C for three hours in a muffle furnace.

Trace element analysis of an aliquot of whole rocks (40 mg) was performed using inductively coupled plasma mass spectrometry (Agilent 7500, Santa Clara, CA, USA) after acid digestion of samples in a HF + HNO_3 flux for 48 h at about 190 °C. The solution was evaporated to incipient dryness, dissolved in concentrated HNO_3, and evaporated at 150 °C to dispel the fluorides. The samples were diluted to about 80 g for analysis after being re-dissolved in 30% HNO_3 overnight. An internal standard solution containing Rh monitored signal drift during ion counting. Analytical results for USGS standards indicated that the uncertainties for most elements were within 5%. The analytical procedures for whole-rock major and trace elements were similar to those described by [27].

4.2. Electron Microprobe Analysis

Major element compositions and BSE images of alkali feldspar and muscovite in carbon-coated thin sections were acquired using an electron probe microanalyzer, JEOL JXA-8100 at the State Key Laboratory of Lithospheric Evolution, Institute of Geology and Geophysics, Chinese Academy of Sciences, Beijing, China. An accelerating voltage of 15 kV, beam current of 10 nA, counting time of 10–30 s on each peak, and a beam diameter of 5 μm were used to carry out routine quantitative analyses. Natural samples and synthetic oxides were used for standard calibration: albite for Na, fluorite for F, $BaSO_4$ for Ba, apatite for P, diopside for Ca, Mg, and Si, $SrSO_4$ for Sr, bustamite for Mn, K-feldspar for K, Al_2O_3 for Al, Fe_2O_3 for Fe, rutile for Ti, Rb glass for Rb and pollucite for Cs. Raw data reduction was undertaken using a routine ZAF procedure. All elements were analyzed at greater than 98% precision. The structural formula for feldspar was calculated based on eight oxygen atoms, and end members were calculated as Or, Ab, and An. The structural formula for the muscovite was calculated based on 24 atoms of O, OH, and F. Li_2O calculation was done after [28], and H_2O calculation was done after [29].

4.3. Laser Ablation Inductively Coupled Plasma Mass Spectrometry

The trace element content of the alkali feldspar and muscovite was determined after removing the carbon coating from the thin sections used for EPMA. The experiment was carried out on an Agilent 7500a Q-ICP-MS instrument (Agilent Technologies, Santa Clara, CA, USA) coupled to a 193 nm ArF excimer laser system (Geolas HD, Lambda Physik, Göttingen, Germany) or an Analyte G2 193 nm ArF excimer laser ablation system at the State Key Laboratory of Lithospheric Evolution, Institute of Geology and Geophysics, Chinese Academy of Sciences. The approach was similar to [30,31], with isotopes measured in peak-hopping mode with a laser beam diameter of ca. 44 μm and a 5 Hz repetition rate. The laser energy density was ~6 J cm^{-2}. Helium was employed as the ablation gas to improve the transporting efficiency of ablated aerosols. NIST SRM 610 reference glass was used as calibration material, and ARM-1 [32] and BCR-2G were analyzed for data quality control. Silicon (^{29}Si) was used as an internal standard, using the Si value determined from EPMA analysis. The raw data were reduced using GLITTER [33]. For most trace elements (>0.10 μg/g), the accuracy was better than ±10%, with analytical precision (1 RSD) of ±10%.

5. Results

5.1. Whole-Rock Chemistry

The major and trace element results for whole rock analysis are presented in Table 2, Supplementary Table S1. Most of the studied rocks plot in the granite field. Some samples from the alkali feldspar-rich zones of Yamrang Pegmatite plot in quartz-monzonite and syenite areas (Figure 5a). Since alkali feldspar has a high K and Na content, the bulk composition falls in the syenite, rather than the granite, field. All rocks analyzed have a peralkaline and

peraluminous nature and plot in the S-type field with ASI index > 1.1 (1.2–3.3) (Figure 5b). The total REE content of studied pegmatite and granite samples ranges from 1 to 161 ppm, while paragneiss samples contain 121–178 ppm total REE (Supplementary Table S1).

Table 2. Whole-rock major and trace element composition of selected pegmatite, gneiss and granite samples.

Lithology	Beryl Pegmatite						Paragneiss		Barren Pegmatite		Leucogranite		Orthogneiss
Sample	Zone 1	Zone 2	Zone 3	Zone 5	WP	SP	YRP-14	IW-7	WPT-88	WPT-112	KGP-20	WPT-205	KGP-6
wt.%													
SiO_2	73.15	79.16	70.22	75.10	73.24	72.36	71.83	81.73	78.28	73.39	73.11	75.76	76.49
Al_2O_3	16.28	11.76	16.14	15.06	14.75	16.63	12.11	7.92	13.05	15.15	14.52	14.10	13.62
TiO_2	0.02	0.05	0.01	0.01	0.03	0.05	0.50	0.22	0.06	0.02	0.14	0.01	0.11
TFe_2O_3	0.39	0.58	0.19	0.27	0.15	0.16	2.21	2.32	0.67	0.47	1.13	0.45	0.47
MgO	0.07	0.05	0.00	0.01	0.06	0.10	2.74	3.15	0.22	0.13	0.23	0.11	0.22
MnO	0.03	0.02	0.09	0.26	0.00	0.00	0.03	0.00	0.02	0.05	0.03	0.03	0.01
CaO	0.51	0.70	0.13	0.47	0.36	2.21	1.58	0.46	0.55	0.57	1.10	0.30	0.56
Na_2O	7.43	3.98	2.73	8.31	2.63	6.52	1.71	2.46	0.92	3.39	3.42	4.22	6.32
K_2O	1.59	3.18	10.11	0.28	7.46	0.54	2.69	1.12	4.35	6.24	4.74	4.47	0.86
P_2O_5	0.16	0.12	0.12	0.13	0.14	0.09	0.05	0.06	0.37	0.17	0.12	0.24	0.15
LOI	0.36	0.39	0.25	0.08	0.51	0.47	4.42	0.51	1.47	0.29	0.84	0.27	0.27
TOTAL	100.0	100.0	100.0	100.0	99.3	99.1	99.9	100.0	100.0	99.9	99.4	100.0	99.1
A/CNK	1.71	1.50	1.25	1.66	1.41	1.79	2.03	1.96	2.24	1.5	1.57	1.57	1.76
µg/g													
Li	16.96	32.39	18.86	7.06	bdl	2.20	14.29	11.33	12.43	68.76	67.51	27.05	12.07
Be	531	8.56	17.37	115	4.01	11.26	2.42	0.45	2.85	1.71	10.82	1.41	0.57
B	0.00	0.00	0.00	0.00	0.00	0.00	0.00	0.00	20.46	76.07	0.00	187	0.00
Sc	1.64	0.66	0.31	0.31	0.09	0.69	11.85	4.57	18.31	1.85	1.47	2.95	4.05
Ti	0.00	0.00	0.00	0.00	113	56.32	0.00	0.00	0.00	0.00	721	0.00	437
V	0.25	0.27	0.11	0.26	4.25	7.09	295	24.53	0.80	1.67	9.83	0.44	5.39
Cr	3.31	1.69	0.93	2.19	0.00	0.00	58.43	25.38	2.83	4.23	0.00	5.28	0.00
Mn	0.00	0.00	0.00	0.00	21.19	29.87	0.00	0.00	0.00	0.00	200	0.00	56.14
Co	0.33	0.70	0.08	0.09	0.44	0.18	2.19	3.71	0.50	0.48	0.92	0.18	0.30
Ni	1.56	0.75	0.63	0.67	0.75	0.82	7.72	9.85	0.47	0.73	0.78	0.47	0.70
Cu	2.32	7.78	1.13	2.16	1.12	1.08	4.77	1.36	2.27	2.37	0.43	2.80	0.15
Zn	12.25	21.78	2.75	3.54	0.07	5.37	123	14.23	10.40	4.63	44.00	7.86	7.65
Ga	12.46	7.52	9.32	14.15	3.98	11.95	17.26	10.10	20.40	11.38	12.90	10.51	13.16
Rb	160	161	1083	17.20	289.10	9.58	133	41.01	181	285	440	141	31.46
Sr	2.02	21.14	1.95	0.61	36.49	88.43	76.74	22.58	35.16	154	65.21	19.94	52.06
Zr	170	3.51	4.86	10.71	20.85	11.80	56.46	57.12	16.59	16.95	69.89	16.37	54.16
Nb	7.90	8.85	8.20	59.61	3.38	1.53	12.48	7.76	20.39	0.89	20.51	1.20	22.88
Mo	0.05	0.01	0.01	0.02	0.05	0.02	11.73	0.07	0.02	0.06	0.16	0.03	0.19
Sn	0.00	0.00	0.00	0.00	6.06	1.64	0.00	0.00	0.00	0.00	21.23	0.00	7.28
Cd	0.24	0.12	0.09	0.34	0.00	0.00	0.10	0.01	0.02	0.09	0.00	0.09	0.00
In	0.01	0.01	0.01	0.01	0.00	0.00	0.07	0.02	0.15	0.04	0.00	0.03	0.00
Cs	53.63	23.10	93.32	6.22	57.45	0.60	6.72	1.84	6.73	5.66	33.95	0.18	1.00
Ba	2.93	32.97	5.51	3.13	1069	28.96	438	93.56	165.47	711.31	193	47.06	24.26
Hf	8.63	0.15	0.28	0.71	1.01	0.50	1.61	1.74	0.57	0.44	3.40	0.44	3.00
Ta	2.83	2.11	1.19	17.12	2.06	0.66	0.86	0.69	1.67	0.13	7.18	0.10	11.52
W	0.86	1.33	0.69	1.34	8.74	3.38	1.46	0.37	22.66	0.23	6.17	0.11	3.26
Tl	1.10	0.83	5.25	0.20	1.52	0.06	1.40	0.15	0.96	1.74	2.63	0.87	0.19
Pb	29.00	66.32	77.25	23.05	68.49	93.78	27.65	3.07	17.64	39.65	76.52	25.87	5.18
Bi	2.52	11.99	4.18	0.76	0.00	0.00	0.44	0.01	0.10	0.06	0.00	0.06	0.00
Th	3.11	1.25	0.80	2.22	1.01	0.62	12.48	15.08	0.47	0.64	14.88	0.15	8.20
U	25.39	3.09	14.76	5.87	9.39	28.66	7.05	3.45	0.93	0.58	50.10	0.86	11.85
µg/g													
Y	37.27	5.06	0.45	4.14	4.59	7.49	17.28	10.71	14.38	2.41	14.88	1.98	12.03
La	6.70	1.46	0.33	1.85	2.24	4.13	38.23	25.62	2.42	3.34	17.83	0.93	3.26
Ce	12.25	2.38	0.51	3.60	4.47	6.44	65.32	46.62	8.00	5.50	35.60	1.76	6.94
Pr	1.40	0.25	0.05	0.37	0.47	0.65	8.95	6.22	0.96	0.43	4.18	0.16	0.85
Nd	4.50	0.81	0.16	1.04	1.61	2.15	29.84	20.04	4.19	1.37	15.22	0.52	3.09
Sm	1.61	0.27	0.04	0.44	0.40	0.54	4.94	3.60	2.19	0.27	3.79	0.16	1.11
Eu	0.04	0.26	0.02	0.01	0.29	1.13	0.89	0.68	0.19	0.78	0.55	0.04	0.14
Gd	1.79	0.30	0.03	0.36	0.51	0.71	4.19	2.97	2.08	0.24	4.37	0.15	1.70
Tb	0.63	0.09	0.01	0.12	0.11	0.20	0.61	0.41	0.57	0.04	0.71	0.04	0.43
Dy	5.70	0.77	0.06	0.75	0.74	1.23	3.05	1.98	3.34	0.29	3.53	0.30	2.44
Ho	1.19	0.15	0.01	0.09	0.17	0.28	0.60	0.35	0.53	0.06	0.63	0.05	0.47
Er	4.24	0.49	0.03	0.20	0.59	0.94	1.64	0.96	1.37	0.18	1.64	0.17	1.36
Tm	1.11	0.12	0.03	0.06	0.10	0.15	0.25	0.12	0.25	0.04	0.22	0.04	0.22
Yb	9.18	0.72	0.04	0.26	0.81	1.06	1.55	0.63	1.57	0.27	1.44	0.31	1.63
Lu	1.61	0.12	0.01	0.04	0.10	0.13	0.22	0.09	0.20	0.04	0.16	0.04	0.21
∑REE	89.2	13.2	1.76	13.3	17.2	27.2	178	121	42.3	15.3	105	6.65	35.9

Note: bdl indicates signal below the detection limit; Zone 1, 2, 3, 4 are from the Yamrang Pegmatite; WP, Wairung Pegmatite; SP, Sang-sabu Pegmatite; Major mineral associations are: Zone 1, albite, quartz, tourmaline; Zone 2, blocky perthitic microcline; Zone 3, musco-vite, microcline, quartz; Zone 5, miarolitic albite, quartz, beryl; WP, graphic quartz & K-feldspar, muscovite; SP, graphic quartz & feld-spar, tourmaline.

The beryl-bearing Ikhabu pegmatites have generally high total alkali contents (14 wt.%) and a high Fe (1.3 wt.%) and Be content (4–531 ppm). Other notable elements include Ca (2.2 wt.%), P (0.5 wt.%), Nb up to 60 ppm, and Ta up to 17 ppm (Table 2). The barren pegmatites have a relatively lower Be content (<4.5 ppm), and a high Nb content (73 ppm) with 13 ppm Ta, 2.4 wt.% Ca, 1.5 wt.% Fe and 0.5 wt.% P. The abundance of Be, Li, Cs, Ta, and Nb in the whole rocks is shown in Figure 6. Enrichments of Be, Cs, and Nb is noted in beryl-bearing Ikhabu pegmatites. Lithium is enriched in orthogneiss (average-34.3, range 12–72 ppm), leucogranite (average-23.3, range 0.7–66 ppm), and barren pegmatite (average-22, range 6–69 ppm) relative to the Ikhabu pegmatites (average-13.3, range-0.7–33 ppm) (Supplementary Table S1). All studied rocks show a higher Nb than Ta content (Figure 6). Among the granitic plutons, two samples of tourmaline-leucogranite (KGP-18 and KGP-20) are enriched in Be (up to 11 ppm), Nb (21 ppm) and Ta (8 ppm) (Figure 6). These leucogranites are also enriched in Fe (~1.2 wt.%) and Ca (~1.2 wt.%), with P (0.1 wt.%), Mg (0.3 wt.%), and Ti (0.1 wt.%). The Be content in other plutons is <3 ppm, although some are richer in Nb (~33 ppm) and Ta (12 ppm). The paragneiss host rocks of Ikhabu pegmatites are rich in Fe (2.3 wt.%), with Ca (1.6 wt.%), Mg (3.2 wt.%), Ti (0.5 wt.%), and P (~0.1 wt.%). The host rock of the Yamrang Pegmatite (YRP-14) contain ~2.4 ppm Be and ~12.5 ppm Nb with low Ta (1 ppm) (Table 2).

Chondrite-normalized REE distribution patterns for the pegmatite samples show LREE enrichments and both negative and positive Eu anomalies (Figure 7a,c). Positive Eu anomalies in some pegmatite samples were probably due to wall rock interaction or weak plagioclase fractionation; however, this does not affect the overall REE trend [34]. Beryl pegmatites have a gentler REE chondrite pattern with a flatter HREE pattern than barren pegmatites (Figure 7a,c). Some beryl pegmatite samples show a positive Tm anomaly.
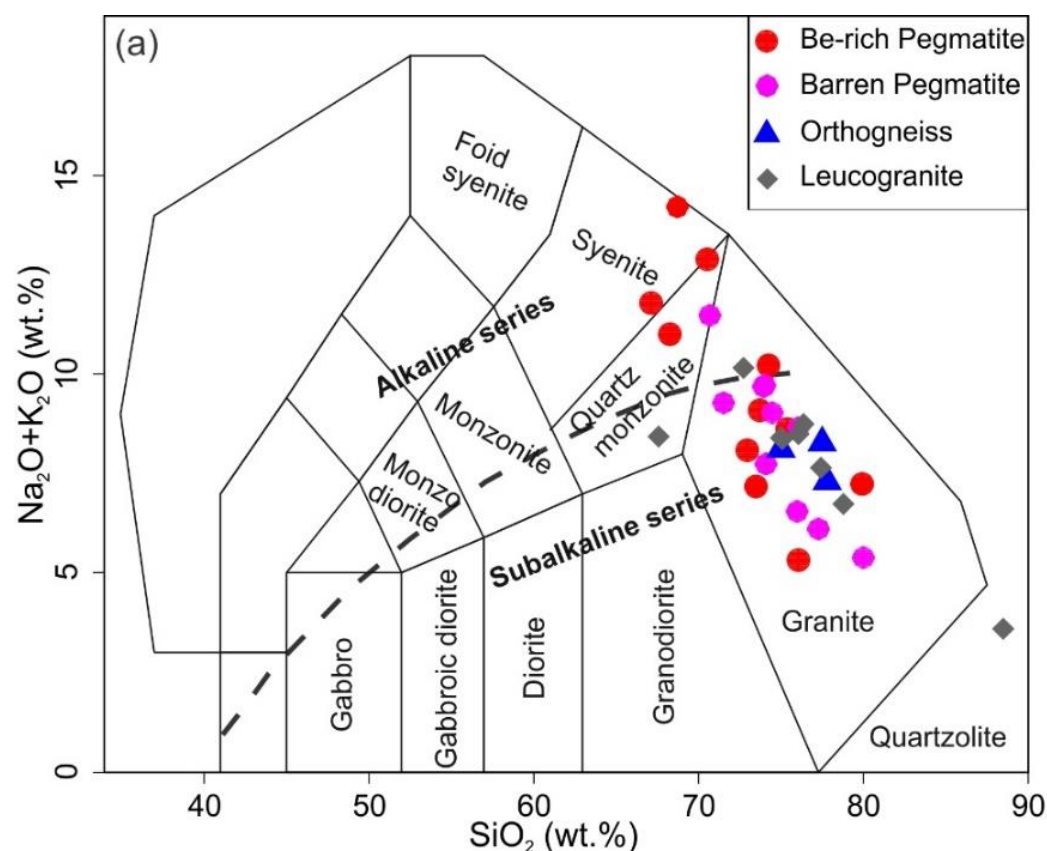

Figure 5. *Cont.*
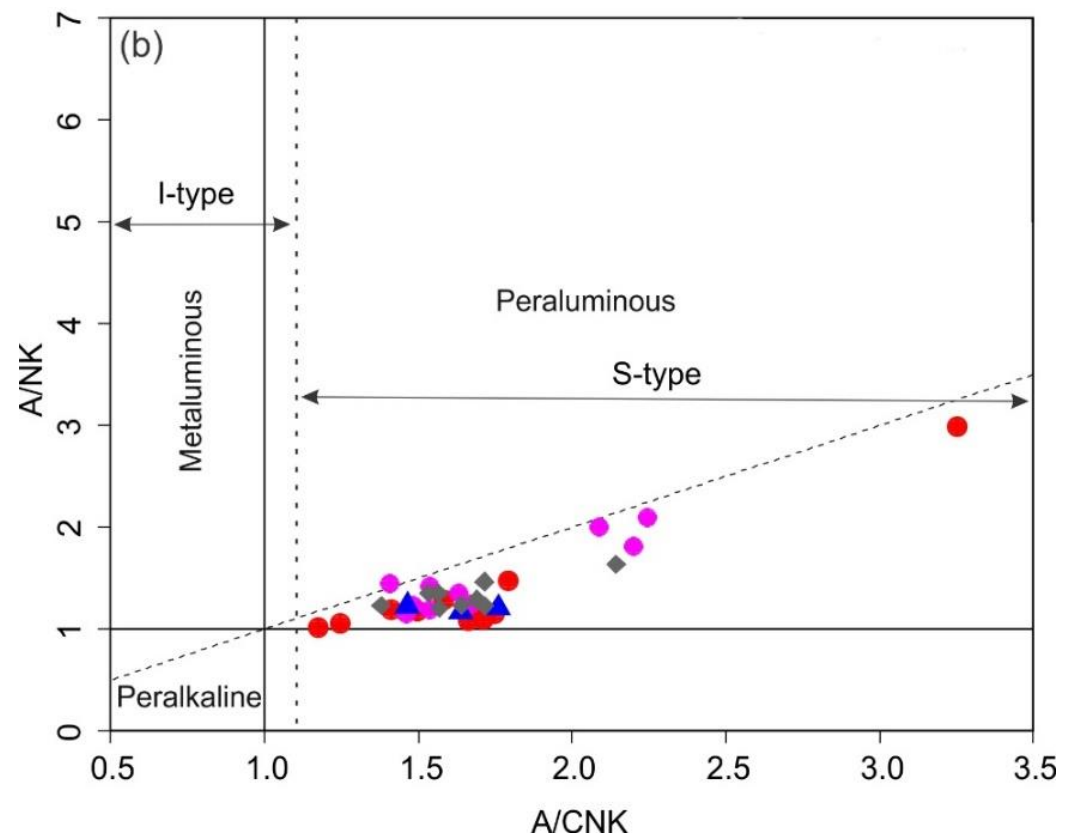
Figure 5. Plots of (**a**) total alkali (Na$_2$O + K$_2$O) vs. SiO$_2$ after [35]. Due to bulk samples being taken from the alkali feldspar-rich zones of the Yamrang Pegmatite, some data plot in the syenite field. (**b**) A/NK vs. A/CNK after [36] of pegmatites and granites from the Higher Himalaya of Eastern Nepal.
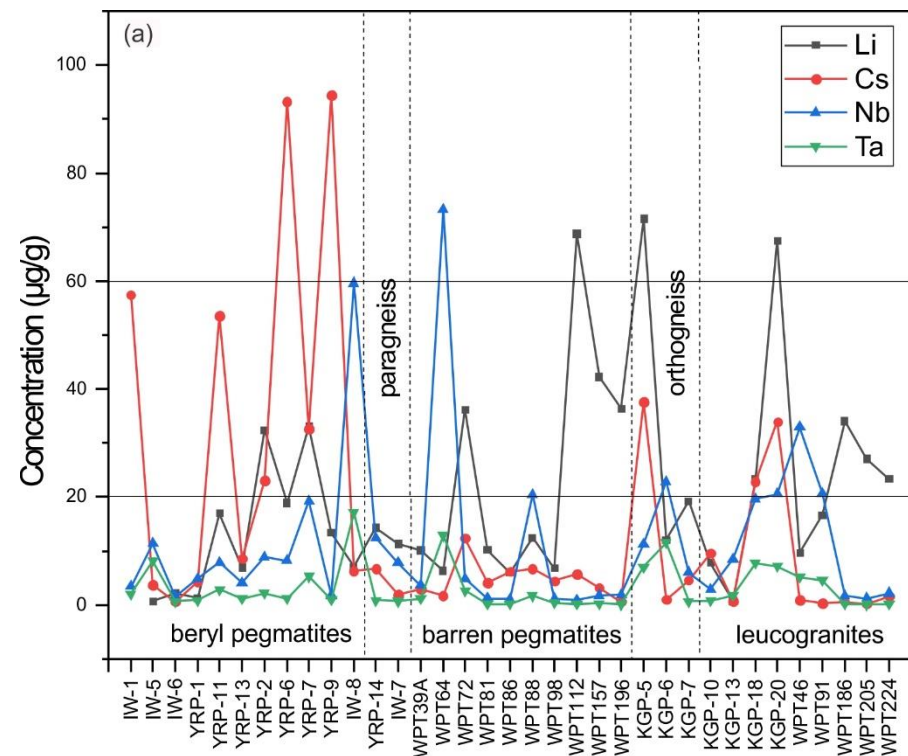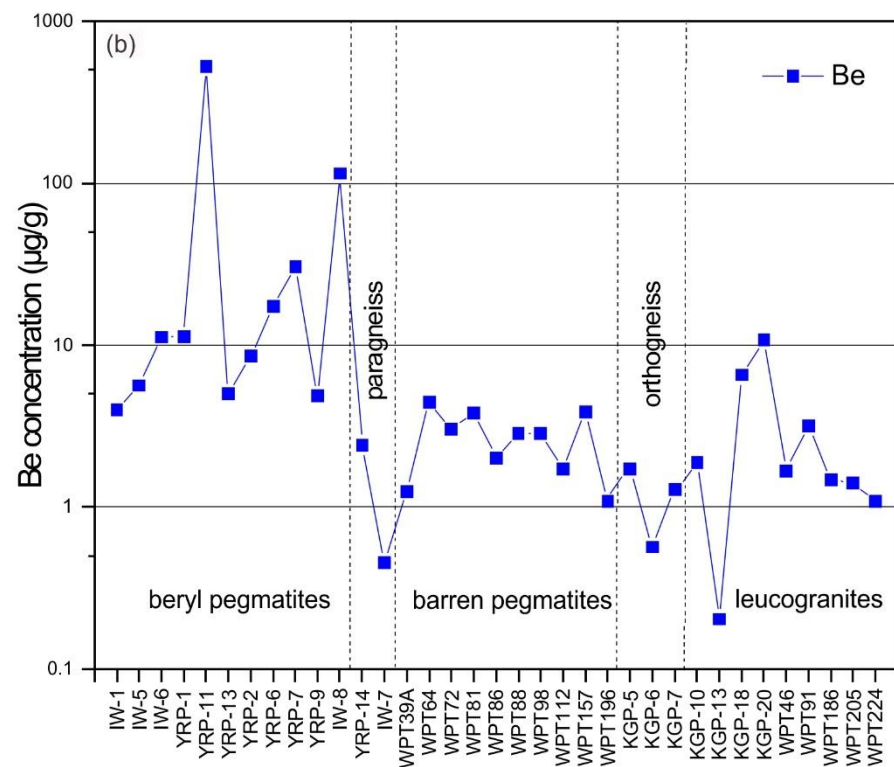

Figure 6. *Cont*.

Figure 6. Concentration profiles of (**a**) Li-, Cs-, Nb-, Ta-; (**b**) Be- in pegmatites, gneiss, and granites from Eastern Nepal, Higher Himalaya.
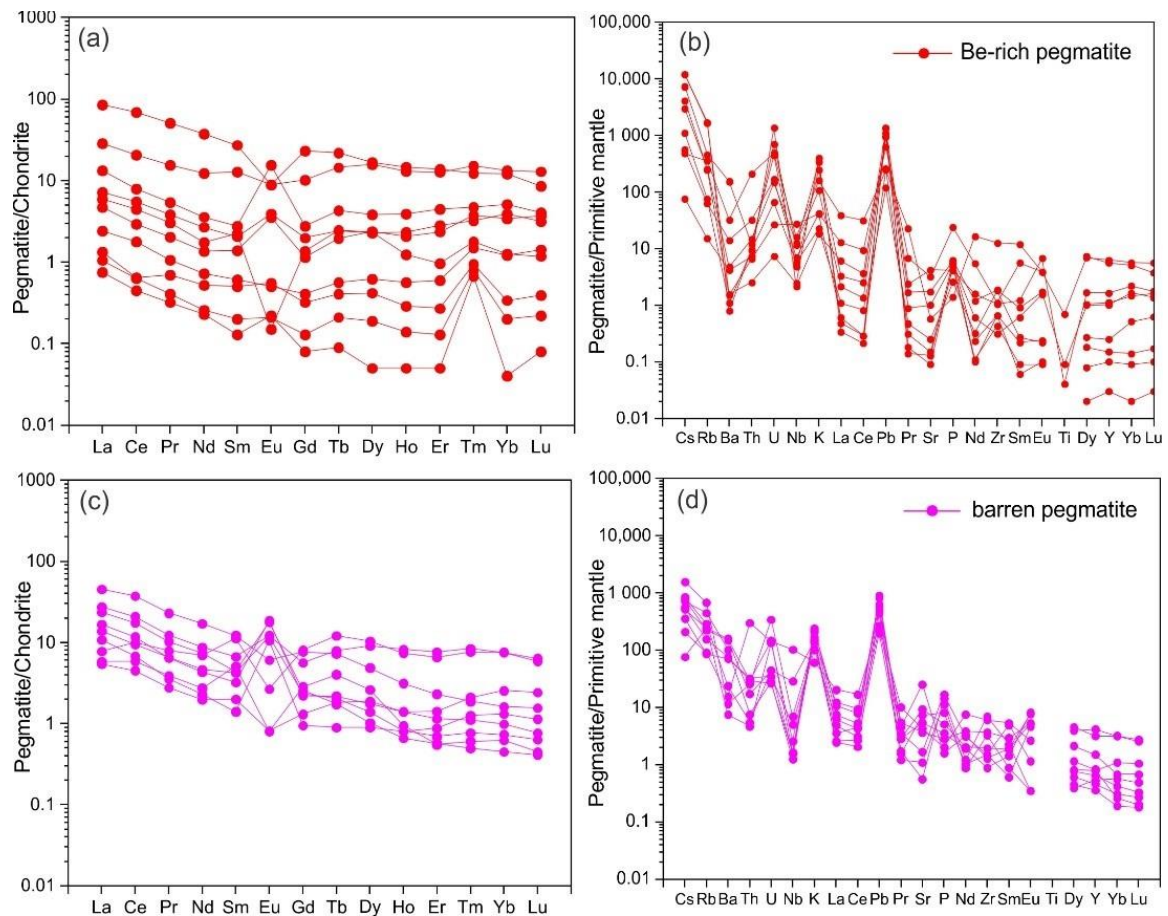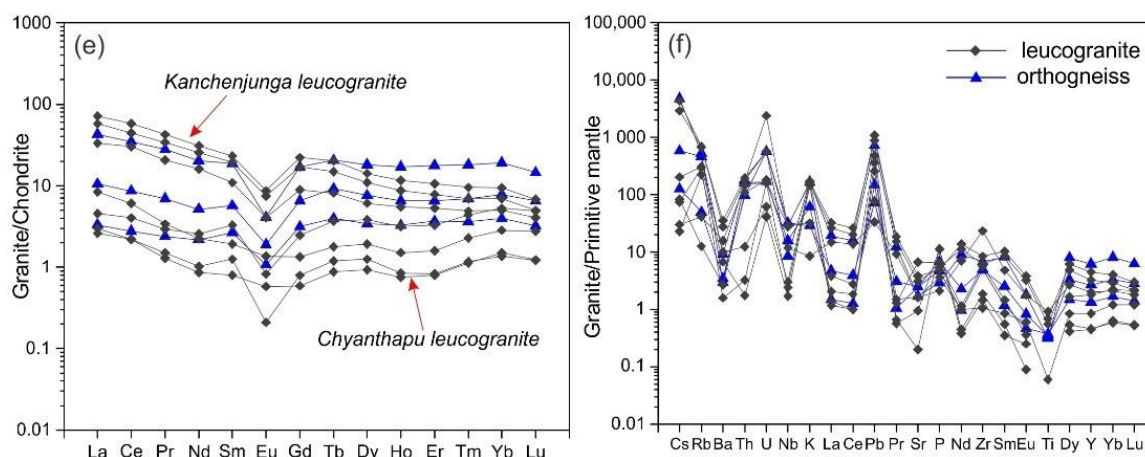

Figure 7. *Cont.*

Figure 7. Chondrite-normalized REE patterns and primitive mantle-normalized multi-element patterns for (**a**,**b**) Be-rich pegmatite; (**c**,**d**) Barren pegmatites, and (**e**,**f**) Orthogneiss and leucogranites. Chondrite values are from [37], and primitive mantle values are from [38].

Chondrite-normalized REE distribution patterns for the leucogranites and orthogneiss samples are similar, showing enrichment of light REE and negative Eu anomalies (Figure 7e). However, the orthogneiss and Chyanthapu leucogranites show a flatter HREE pattern than the Kanchenjunga leucogranites (Figure 7e).

The primitive mantle normalized multi-element diagrams for beryl-pegmatites, barren pegmatites, leucogranites, and orthogneiss show a depletion of Ba, Nb, Sr, and moderate to strong enrichment of Cs, Rb, U, K, Pb (Figure 7b,d,f). Beryl pegmatites have a steeper normalized multi-element pattern than barren pegmatites, leucogranites, and orthogneiss, with stronger element enrichments and depletions (Figure 7b).

5.2. Feldspar Chemistry

Feldspars were sampled and analyzed from all five zones of the Yamrang Pegmatite. Samples YRP-1A, YRP-11A, YRP-13A were from zone 1; YRP-2B, YRP-12A from zone 2, YRP-4, YRP-9A from zone 3, and YRP-7E was from zone 5. YRP-8B is the microcline sample from the core margin associated with quartz and beryl. We have assigned it to core zone 4. The feldspar in samples from zones 1 and 5 is albite, while zones 2, 3, and 4 contain perthitic microcline (Figure 8). Feldspar samples show a homogeneous texture in BSE images.

Endmembers were determined in terms of Ab, An, and Or using feldspar major element data from various zones. The representative major element contents are shown in Table 3, and a full set of data is provided in Supplementary Table S2. The alkali feldspars from zones 1 and 5 were albite (Na-alkali feldspar), and those from zones 2, 3, and 4 were perthitic microcline (K-alkali feldspar). Alkali feldspar from zone 1 has a higher An component (An_{9-12}), while the innermost part (core) has the lowest An ($An_{0.1-0.7}$) (Figure 9). Albite from zone 1 consists of Ab_{87-100}, An_{0-12}, Or_{0-2}. The albite sample from zone 5 is Ab_{96-98}, An_{2-4}, $Or_{0.5-1}$, whereas the microcline composition from zone 2 is Ab_{10-98}, An_{0-2}, Or_{1-91}. Zone 3 feldspar is Ab_{10-99}, An_{0-2}, Or_{1-90} and zone 4 is Ab_{12-99}, An_{0-1}, Or_{1-88} (Figure 9).

The average trace element data for the alkali feldspar (excluding the albite phase from perthitic microcline) is presented in Table 4, and the full set of data is given in Supplementary Table S3. Alkali feldspar from the Yamrang Pegmatite consists of average contents of K-42,479 ppm (range 114–165,414 ppm), Rb-543 ppm (range 1–2925 ppm), Cs-46 ppm (range 0–323 ppm), P-293 ppm (range 22–906 ppm), Ga-11.4 ppm (range 1–30 ppm), Nb < 1 ppm, Ba-179 ppm (range 1–462 ppm), and Ta below the limit of detection. The K/Rb values range from 46 to 1265, with K/Cs, Rb/Sr and Nb/Ta values of 375–13,259, 0–2259, and 3–20, respectively (Figure 10, Supplementary Table S3). The Cs vs. K/Rb plot for alkali feldspar shows an overall negative correlation between K/Rb and Cs, and data reach the Be-pegmatite field (Figure 10a). The median K/Cs value for alkali feldspar decreases from

zones 2 to 5, with zone 1 and 3 being similar. The median K/Rb value also decreases from zones 1 to 5, with zone 5 being slightly higher than zone 4. The median Nb/Ta and Rb/Sr increase from zone 1 to 4 but Rb/Sr decreases in zone 5 (Figure 10).
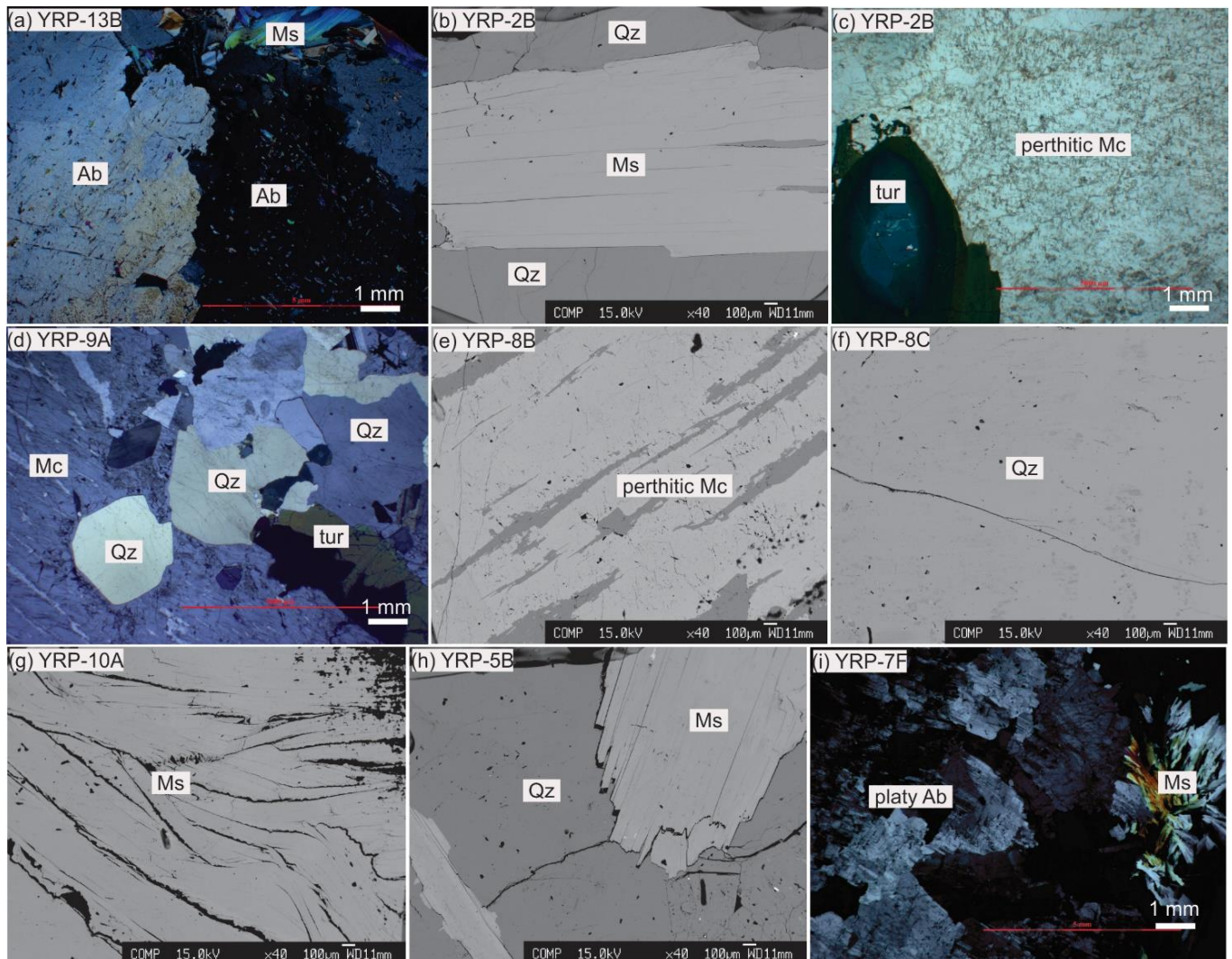

Figure 8. Photomicrographs and BSE images of alkali feldspar, muscovite, and quartz from the Yamrang Pegmatite. (**a**) Assemblage of albite, primary muscovite, and secondary mica overgrowing albite from zone 1 under cross-polarized light; (**b**) BSE image of homogeneous muscovite and quartz from zone 2; (**c**) Perthitic microcline and tourmaline from zone 2 under plane-polarized light; (**d**) Assemblage of perthitic microcline, anhedral quartz, and tourmaline from zone 3 under cross-polarized light; (**e**) BSE image of perthitic microcline from zone 4; (**f**) BSE image of homogeneous quartz from the core; (**g**) BSE image of muscovite sampled near core zone 4; (**h**) BSE image of miarolitic homogeneous muscovite and quartz; (**i**) Platy albite and muscovite books assemblage from miaroles under cross-polarized light. Mineral abbreviations: Ab, albite; Mc, microcline; Ms, muscovite; Qz, quartz; Tur, tourmaline. Mineral abbreviations are after [10].

Table 3. The representative EPMA major element composition of alkali feldspar from the Yamrang Pegmatite, Ikhabu Pegmatite Field (IPF), Eastern Nepal.

	Zone 1 (Marginal Zone)			Zone 2 (Outer IZ)		Zone 3 (Inner IZ)			Zone 4 (Core)		Zone 5 (Miarolitic Zone)	
	Albite			Microcline		Microcline			Microcline		Albite	
Sample	YRP-1A-F1	YRP-1A-F2	YRP-1A-F3	YRP-12A-F1	YRP-12A-F5	YRP-6A-F1	YRP-4-F2	YRP-9A-F1	YRP-8B-F2	YRP-8B-F5	YRP-7B-F2	YRP-7B-F3
SiO_2 (wt%)	65.16	65.04	64.86	63.82	64.44	64.60	65.36	64.47	64.30	64.32	67.86	68.22
TiO_2	0.00	0.00	0.00	0.00	0.00	0.03	0.00	0.04	0.00	0.00	0.00	0.00
Al_2O_3	20.93	21.02	20.91	17.72	18.23	17.99	18.19	17.71	18.01	17.91	19.56	18.86
FeO	0.01	0.00	0.06	0.00	0.00	0.02	0.01	0.00	0.01	0.02	0.01	0.00
MnO	0.00	0.00	0.00	0.00	0.02	0.03	0.00	0.00	0.02	0.03	0.00	0.00
MgO	0.00	0.01	0.00	0.00	0.00	0.00	0.00	0.00	0.00	0.00	0.03	0.02
CaO	2.56	2.50	2.49	0.01	0.00	0.04	0.04	0.00	0.05	0.01	0.78	0.36
Na_2O	10.65	10.59	10.66	1.47	1.00	1.06	1.16	1.32	1.58	1.30	11.67	12.03
K_2O	0.20	0.13	0.30	13.60	14.57	14.54	14.12	14.04	13.87	13.94	0.17	0.09
Total	99.52	99.28	99.28	96.61	98.26	98.30	98.89	97.58	97.84	97.54	100.07	99.59
Oxygen atoms = 8												
Si (apfu)	2.870	2.873	2.863	3.042	3.027	3.033	3.051	3.045	3.023	3.040	2.960	2.984
Ti	0.000	0.000	0.000	0.000	0.000	0.001	0.000	0.001	0.000	0.000	0.000	0.000
Al	1.087	1.094	1.088	0.995	1.009	0.995	1.001	0.986	0.998	0.998	1.005	0.972
Fe	0.000	0.000	0.002	0.000	0.000	0.001	0.001	0.000	0.000	0.001	0.000	0.000
Mn	0.000	0.000	0.000	0.000	0.001	0.001	0.000	0.000	0.001	0.001	0.000	0.000
Mg	0.000	0.001	0.000	0.000	0.000	0.000	0.000	0.000	0.000	0.000	0.002	0.001
Ca	0.121	0.118	0.118	0.001	0.000	0.002	0.002	0.000	0.002	0.001	0.036	0.017
Na	0.910	0.907	0.912	0.136	0.091	0.097	0.105	0.121	0.144	0.119	0.987	1.020
K	0.011	0.007	0.017	0.827	0.872	0.870	0.841	0.846	0.831	0.840	0.009	0.005
Total	5.000	5.000	5.000	5.000	5.000	5.000	5.000	5.000	5.000	5.000	5.000	5.000
End members												
Ab	87.29	87.85	87.12	14.08	9.48	9.97	11.06	12.51	14.75	12.38	95.59	97.91
An	11.61	11.44	11.26	0.06	0.01	0.19	0.20	0.00	0.25	0.05	3.51	1.63
Or	1.10	0.70	1.62	85.85	90.51	89.84	88.74	87.49	85.00	87.57	0.90	0.46

Note: IZ, Intermediate zone; structural formulae were calculated based on 8 No. of oxygen.
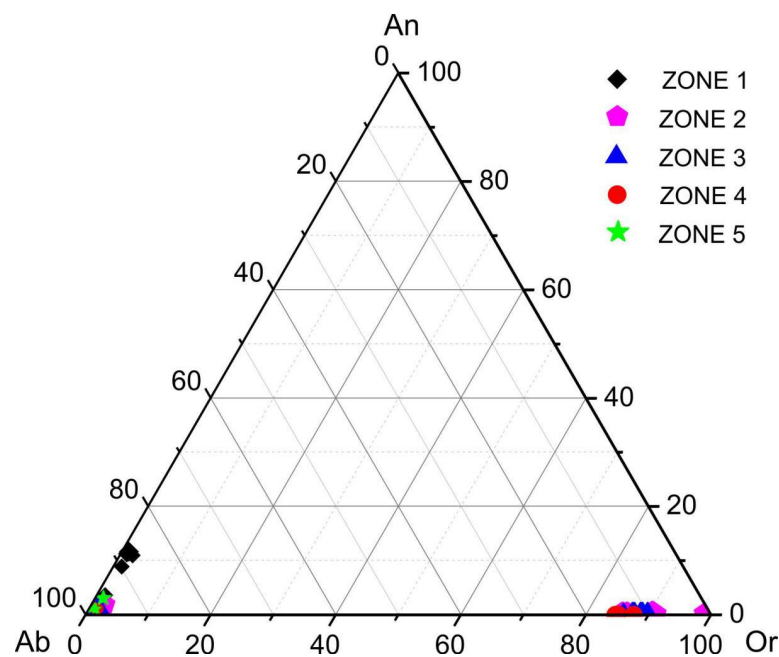

Figure 9. The ternary diagram of Ab-An-Or composition of alkali feldspar from five zones of the Yamrang Pegmatite.

Table 4. The average LA-ICP-MS trace element composition of alkali feldspar from the Yamrang Pegmatite, Ikhabu Pegmatite Field (IPF), Eastern Nepal.

	Zone 1 (Marginal Zone)				Zone 2 (Outer IZ)				Zone 3 (Inner IZ)				Zone 4 (Core)				Zone 5 (Miarolitic Zone)			
Phase	Albite				Microcline				Microcline				Microcline				Albite			
	n = 16				n = 5				n = 5				n = 3				n = 5			
Element	Avg	Min	Max	σ	Avg	Min	Max	σ	Avg	Min	Max	σ	Avg	Min	Max	σ	Avg	Min	Max	σ
Li (ppm)	2.31	1.27	4.27	0.81	6.30	3.66	11.1	2.88	24.2	3.47	48.7	19.8	48.6	19.9	69.0	25.6	-	bdl	bdl	-
Be	5.61	1.27	10.4	3.42	5.29	4.36	7.15	1.19	5.51	3.48	8.52	2.32	4.12	3.94	4.40	2.28	13.3	11.3	15.7	1.71
B	22.5	11.4	43.8	8.7	26.7	21.1	37.5	7.5	38.1	27.3	49.0	15.4	-	bdl	bdl	-	-	bdl	bdl	-
P	84.5	41.5	215	52.3	376	307	405	40.2	479	308	599	108	695	671	709	263	841	794	906	40.5
K/10³	2.33	0.65	3.91	1.18	148	143	154	4.19	132	90.8	165	30.7	139	134	143	65.5	6.19	1.19	15.4	5.94
Ti	98.2	5.5	156	40.9	6.8	5.10	9.7	1.99	20.2	3.6	47.7	24.0	5.91	5.91	5.91	49.8	4.46	3.81	5.10	0.91
Ga	8.24	1.21	18.7	5.81	12.6	11.6	14.0	0.94	13.0	10.3	14.9	1.7	18.6	14.0	21.1	6.93	28.8	27.6	30.2	1.13
Rb	5.87	0.94	11.3	3.11	937	884	977	33.8	1272	816	1669	320	2697	2417	2925	980	72.8	2.08	177	78.9
Sr	119	6.33	237	83.7	22.7	17.0	34.3	6.7	17.0	1.0	69.2	29.2	5.01	1.07	7.35	64.6	0.94	0.52	1.74	0.49
Nb	0.55	0.40	0.79	0.14	0.25	0.22	0.28	0.04	-	bdl	bdl	-	-	bdl	bdl	-	-	bdl	bdl	-
Sn	2.95	0.76	6.92	1.79	4.30	3.46	4.89	0.75	4.56	4.14	4.99	0.37	7.76	5.57	9.06	2.18	2.16	2.16	2.16	-
Sb	1.06	0.35	2.70	0.73	-	bdl	bdl	-	-	bdl	bdl	-	0.92	bdl	bdl	-	1.63	1.47	1.78	0.22
Cs	0.48	0.45	0.54	0.04	19.1	12.7	40.6	12.1	95.4	13.5	323	131	106	82.9	122	104	22.7	5.95	41.0	17.6
Ba	217	0.92	462	151	71	43.4	95	19.0	41.1	1.72	145	59.6	29.9	29.8	30.0	112	21.1	bdl	bdl	-
La	5.04	2.80	8.00	1.90	0.14	0.12	0.17	0.02	0.68	0.11	2.11	0.96	-	bdl	bdl	-	0.71	0.32	1.66	0.55
Ce	7.93	3.76	13.0	3.24	0.13	0.11	0.15	0.03	0.88	0.06	3.81	1.64	0.07	0.07	0.07	3.23	0.85	0.25	2.21	0.78
Ta	0.08	0.05	0.19	0.05	-	bdl	bdl	-	-	bdl	bdl	-	-	bdl	bdl	-	-	bdl	bdl	-
Pb	23.5	1.02	153	44.7	186	167	236	28.4	158	118	194	35.8	133	113	167	64.1	58.7	38.9	98.3	24.1
K/Rb	540	345	1265	227	158	153	162	3.98	105	87.7	121	12.6	52.1	45.9	59.0	42.6	338	86.7	1017	454
K/Cs	4067	1439	7238	2554	9426	3683	12,052	3315	4091	387	6731	2824	1361	1101	1721	2309	455	375	566	99.5
Nb/Ta	7.16	2.70	10.0	2.23	-	-	-	-	-	-	-	-	-	-	-	-	-	-	-	-
Rb/Sr	0.06	0.01	0.23	0.05	43.5	27.6	52.0	9.39	425	11.8	1196	452	1024	398	2259	627	65.0	4.00	169	71.9

Note: IZ, Intermediate zone; σ, one standard deviation; bdl, below detection limit for the utilized method; -, value could not be determined. The data of albite phase of perthitic microcline from zone 2–4 are excluded in this table but are provided in Supplementary Table S3.
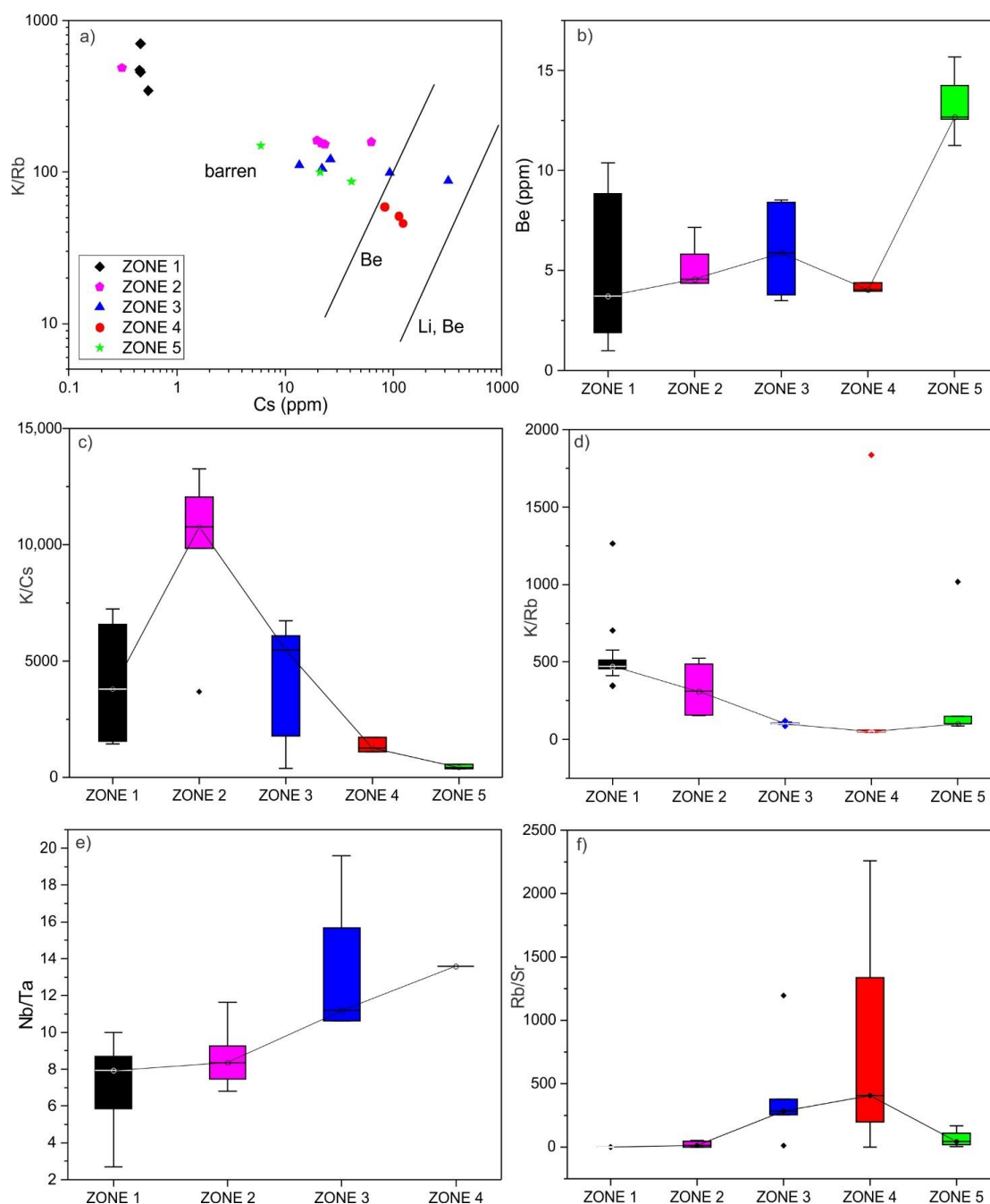
Figure 10. (**a**) Plot of K/Rb vs. Cs (ppm); Box and whisker plots of (**b**) Be; (**c**) K/Cs; (**d**) K/Rb; (**e**) Nb/Ta; (**f**) Rb/Sr of alkali feldspar from five zones of the Yamrang Pegmatite. Connecting lines join the median value. Ratios are calculated as ppm/ppm. Discrimination lines of barren, Be-, and Li, Be- pegmatites are from [39] as presented in [40].

At the magmatic stage, the Be content in alkali feldspar roughly decreases from outer to inner zones (zone 1–4), with an average of 5.6 ppm (range 1–10 ppm) in zone 1, 5.3 ppm (range 4–7 ppm) in zone 2, 5.5 ppm (range 3.5–8.5 ppm) in zone 3, and approximately 4 ppm in zone 4 (Figure 10b, Supplementary Table S3). The miarolitic albite from zone 5 (representing the hydrothermal stage) has the highest Be content of 11–16 ppm, higher than that in the zones representing the magmatic stage (zones 1–4) (Figure 10b). The Be content is higher in alkali feldspar from zone 1 (up to 10 ppm), and this zone also has the highest An component (An_{9-12}) among all magmatic zones (zone 1–4). Be in alkali feldspar shows a strong positive correlation with Cl, Cr, Ga (r > 0.7) and a strong negative correlation with V, Ni (r < −0.7).

5.3. Muscovite Chemistry

Muscovite was sampled from different zones of the Yamrang Pegmatite (Figure 8); however, muscovite was not obtained from the core zone 4. Sample YRP-10A represents the innermost part of zone 3, closest to the core zone. Sample YRP-13B was from zone 1, YRP-2B was from zone 2, YRP-6A and YRP-10A were from zone 3, and YRP-5B and YRP-7F were from zone 5. The zone 1 sample shows secondary muscovite overgrowing albite (Figure 8a), while other samples show primary muscovite. Muscovite has a homogeneous texture in BSE images.

Representative muscovite major and trace element data from different zones of the Yamrang Pegmatite are shown in Tables 5 and 6. The full set of data are given in Supplementary Tables S4 and S5. The Mg-Li vs. Fe+Mg+Ti-Al^{VI} diagram for mica [41] in Figure 11a shows the composition of muscovite from the Yamrang Pegmatite. In Figure 11b, the Fe/(Fe+Mg) vs. Al plot shows that all analyzed muscovite was primary.

Table 5. The representative EPMA major element composition of muscovite from the Yamrang Pegmatite, Ikhabu Pegmatite Field (IPF), Eastern Nepal.

Sample	Zone 1 (Marginal Zone)		Zone 2 (Outer IZ)		Zone 3 (Inner IZ)		Zone 4 (Core)		Zone 5 (Miarolitic Zone)	
	YRP-13B-M1	YRP-13B-M2	YRP-2B-M1	YRP-2B-M2	YRP-6A-M1	YRP-6A-M2	YRP-10A-M1	YRP-10A-M2	YRP-5B-M1	YRP-7F-M2
SiO_2	47.08	47.95	46.98	47.15	48.25	47.87	46.19	47.00	47.29	47.77
TiO_2	0.13	0.22	0.20	0.24	0.11	0.12	0.16	0.13	0.13	0.51
Al_2O_3	32.19	32.10	33.12	32.88	34.88	34.90	32.94	33.35	33.55	32.69
FeO	2.41	2.29	2.36	2.30	2.01	1.94	1.91	1.93	1.90	2.15
MnO	0.12	0.07	0.05	0.09	0.05	0.09	0.05	0.05	0.04	0.04
MgO	0.87	1.17	1.12	1.10	0.47	0.42	0.94	0.83	0.85	0.94
CaO	0.01	0.01	0.00	0.00	0.01	0.00	0.04	0.00	0.04	0.04
Na_2O	0.33	0.42	0.74	0.64	0.87	0.82	0.84	0.71	0.57	0.56
K_2O	9.53	9.39	9.08	9.13	9.09	9.13	9.26	9.40	9.30	9.34
F	0.25	0.51	0.18	0.21	0.23	0.30	0.41	0.23	0.30	0.19
Cl	0.00	0.01	0.01	0.00	0.01	0.00	0.00	0.00	0.00	0.00
Cr_2O_3	0.02	0.00	0.00	0.01	0.01	0.01	0.00	0.00	0.00	0.02
NiO	0.02	0.00	0.01	0.01	0.00	0.05	0.00	0.00	0.01	0.03
Li_2O*	0.00	0.08	0.00	0.00	0.00	0.02	0.05	0.00	0.02	0.00
H_2O*	4.27	4.21	4.36	4.34	4.45	4.40	4.19	4.33	4.31	4.38
Subtotal	97.24	98.43	98.22	98.10	100.45	100.08	96.98	97.96	98.31	98.66
O=F,Cl	0.11	0.22	0.08	0.09	0.10	0.12	0.17	0.10	0.13	0.08
Total	97.13	98.21	98.15	98.02	100.35	99.95	96.81	97.86	98.18	98.58
Structural formulae based on O, OH, F = 24										
Si	6.43	6.46	6.34	6.37	6.34	6.32	6.32	6.35	6.36	6.41
Al iv	1.57	1.54	1.66	1.63	1.66	1.68	1.68	1.65	1.64	1.59
Y										
Al vi	3.61	3.56	3.61	3.60	3.74	3.75	3.63	3.67	3.68	3.58
Ti	0.01	0.02	0.02	0.02	0.01	0.01	0.02	0.01	0.01	0.05
Cr	0.00	0.00	0.00	0.00	0.00	0.00	0.00	0.00	0.00	0.00
Fe	0.28	0.26	0.27	0.26	0.22	0.21	0.22	0.22	0.21	0.24
Mn	0.01	0.01	0.01	0.01	0.01	0.01	0.01	0.01	0.00	0.00
Mg	0.18	0.23	0.23	0.22	0.09	0.08	0.19	0.17	0.17	0.19
Ni	0.00	0.00	0.00	0.00	0.00	0.00	0.00	0.00	0.00	0.00
Li*	0.00	0.04	0.00	0.00	0.00	0.01	0.03	0.00	0.01	0.00
X										
Ca	0.00	0.00	0.00	0.00	0.00	0.00	0.01	0.00	0.01	0.01
Na	0.09	0.11	0.19	0.17	0.22	0.21	0.22	0.19	0.15	0.15
K	1.66	1.61	1.56	1.57	1.52	1.54	1.62	1.62	1.60	1.60
OH*	3.89	3.78	3.92	3.91	3.90	3.88	3.82	3.90	3.87	3.92
F	0.11	0.22	0.08	0.09	0.10	0.12	0.18	0.10	0.13	0.08
TOTAL	17.84	17.85	17.88	17.86	17.82	17.83	17.94	17.88	17.84	17.82
Y total	4.09	4.13	4.13	4.12	4.07	4.08	4.09	4.07	4.09	4.07
X total	1.75	1.73	1.76	1.74	1.75	1.75	1.84	1.81	1.75	1.75
Al total	5.18	5.10	5.27	5.23	5.40	5.43	5.31	5.31	5.32	5.17
Fe/Fe+Mg	0.61	0.52	0.54	0.54	0.70	0.72	0.53	0.57	0.56	0.56
Fe+Mg+Al^{iv}+Ti	4.07	4.07	4.12	4.11	4.07	4.06	4.06	4.07	4.08	4.06
Mg-Li	0.18	0.19	0.23	0.22	0.09	0.07	0.16	0.17	0.16	0.19
Fe+Mg+Ti-Al^{vi}	−3.14	−3.04	−3.09	−3.10	−3.42	−3.44	−3.21	−3.27	−3.28	−3.10

Note: IZ, Intermediate zone; *, calculated from stoichiometry; Li_2O* calculation after [28]; H_2O* calculation after [29].

Table 6. The average LA-ICP-MS trace element composition of muscovite from the Yamrang Pegmatite, Ikhabu Pegmatite Field (IPF), Eastern Nepal.

Element	Zone 1 (Marginal Zone) n = 16				Zone 2 (Outer IZ) n = 5				Zone 3 (Inner IZ) n = 5				Zone 4 (Core) n = 3				Zone 5 (Miarolitic Zone) n = 5			
	Avg	Min	Max	σ	Avg	Min	Max	σ	Avg	Min	Max	σ	Avg	Min	Max	σ	Avg	Min	Max	σ
Li (ppm)	526	432	593	84.0	360	329	392	20.1	282	256	327	24.3	535	519	558	16.5	567	480	696	62.9
Be	30.3	29.9	30.8	0.49	23.2	18.3	28.0	2.94	29.4	25.6	33.4	2.84	29.8	21.0	46.9	10.6	28.8	24.3	32.0	2.71
B	154	109	199	44.7	167	114	195	29.1	200.5	193.5	205.4	4.57	162	131	200	28.5	140	119	167	14.5
Na	4237	3562	4928	683	4145	3473	4488	325	5459	5367	5546	63.6	5436	4114	6869	981	4259	3238	5081	599
Mg	4521	3939	4847	505	4883	4553	5219	248	2233	2159	2393	75.7	5079	4543	5738	486	5184	4512	5851	498
P	77.5	67.3	88.5	10.6	65.2	55.1	72.8	9.12	63.2	52.6	81.8	11.0	82.6	57.5	101	22.4	87.9	71.6	113	14.6
K/10^3	110	110	110	0.29	109	108	111	1.22	103	100	105	2.04	104	99	113	5.51	127	122	136	5.02
Sc	14.2	13.9	14.9	0.55	18.4	13.5	20.3	2.3	15.6	15.0	16.2	0.48	15.0	11.3	18.0	2.88	10.5	2.64	20.8	7.95
Ti	1009	749	1248	250	1197	1128	1286	57.0	706	678	732	16.1	1016	902	1240	146	2574	1176	4491	1485
Mn	460	410	489	44.0	275	248	297	22.9	421	406	439	10.5	428	360	524	70.5	674	515	986	171
Fe	15,337	14,085	15,997	1086	15,394	14,500	16,072	544	15,229	14,521	15,752	402	14,695	12,833	16,168	1575	21,384	16,703	29,575	4730
Zn	73.1	54.4	89.3	17.5	55.6	48.4	65.4	6.3	104	95.0	120	7.8	62.6	18.9	75.3	24.4	98.8	59.7	203	41.3
Ga	128	112	159	26.5	90.5	87.4	92.5	1.8	146	141	151	3.1	117	106	125	8.29	155	134	181	18.2
Rb	2475	1540	4057	1377	920	774	1354	196	2125	2056	2202	49	1525	1480	1561	40.8	4398	2172	6881	2288
Sr	0.73	0.42	0.97	0.28	1.5	0.9	2.0	0.4	0.47	0.18	0.77	0.30	-	bdl	bdl	-	0.44	0.35	0.56	0.07
Zr	1.60	0.54	3.28	1.47	2.5	1.4	3.1	0.6	1.29	1.00	1.85	0.29	2.75	1.84	4.20	0.93	2.22	1.74	2.55	0.25
Nb	296	186	367	96.5	87.6	68.7	142	24.4	245	236	252	6.64	158	136	182	18.0	450	213	701	234
In	1.15	0.45	1.95	0.75	0.5	0.3	0.8	0.2	0.73	0.50	0.96	0.15	-	bdl	bdl	-	2.05	0.61	3.58	1.41
Sn	246	73.5	473	205	87.4	63.3	154	31.4	140	133	144	4.48	68.4	58.7	84.5	12.8	491	113	880	385
Cs	188	47.6	390	179	37.1	13.8	121	39.9	63.6	61.9	66.2	1.48	32.6	30.7	34.4	1.46	310	54.0	621	264.8
Ba	29.3	21.1	34.1	7.16	26.3	18.8	49.6	10.5	-	bdl	bdl	-	10.6	2.68	17.7	7.85	3.32	1.14	6.77	2.14
Ta	103	43.6	176	66.9	12.4	4.9	45.0	14.6	15.1	13.9	15.9	0.80	14.5	9.8	22.4	5.13	90.8	17.9	174	72.1
W	38.3	28.4	44.4	8.68	46.6	42.6	49.8	2.7	42.1	38.1	44.6	2.26	41.5	32.2	61.8	11.6	49.0	45.4	53.4	2.7
Pb	9.7	6.9	11.9	2.6	13.7	12.2	15.2	0.9	7.52	6.97	7.95	0.36	12.1	9.7	15.5	2.34	16.3	12.8	20.5	2.4
K/Rb	52.8	27.2	71.2	22.9	122	80.7	140	19.6	48.4	47.8	49.9	0.71	68.0	63.2	72.9	3.55	38.9	18.0	59.9	21.2
K/Cs	1150	282	2305	1042	5270	906	7900	2801	1618	1573	1675	36.5	3184	2961	3423	199	1207	199	2375	1044
Nb/Ta	3.4	1.9	4.3	1.3	11.0	3.1	15.9	4.4	16.2	15.3	17.0	0.69	11.6	8.15	13.8	2.42	7.3	4.0	12.9	3.4
Rb/Sr	3369	2258	4183	997	624	389	937	182	6434	2751	11,837	4781	-	-	-	-	10,070	4309	19,660	5700

Note: IZ, Intermediate zone; σ, one standard deviation; bdl, below detection limit; -, value could not be determined.
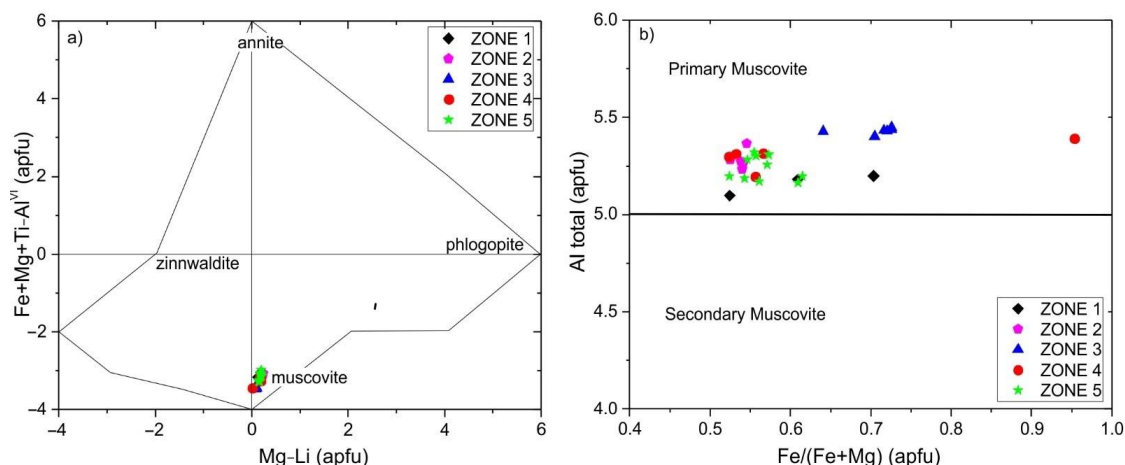
Figure 11. (**a**) Fe+Mg+T-Al^{VI} vs. Mg-Li diagram of mica showing the position of muscovite of Yamrang Pegmatite [41]; (**b**) Total Al (apfu) vs. Fe/(Fe+Mg) diagram of muscovite from Yamrang Pegmatite. The discrimination line of primary and secondary muscovite is from [42].

The K/Rb value ranges from 18 to 140, K/Cs from 199 to 7900, Rb/Sr from 170 to 19,660, and Nb/Ta from 2 to 17 (Table 6). In Figure 12a, the Cs vs. K/Rb plot of muscovite shows an overall negative correlation between K/Rb and Cs, and data points are distributed between Mus-class and REL-class pegmatites. In Figure 12b, the Be vs. K/Rb plot of muscovite shows few data points falling in the REL-class pegmatite field. Muscovites from the miarolitic zone are the most enriched in Be and Cs. The median Be content of muscovite fluctuates less in all zones, ranging from 23 to 30 ppm (Figure 12c). The median muscovite K/Rb and K/Cs value decreases from zones 2 to 5 (Figure 12d,e). The Nb/Ta ratio is highest at zone 3, corresponding to columbite-tantalite mineralization (Figure 12f).
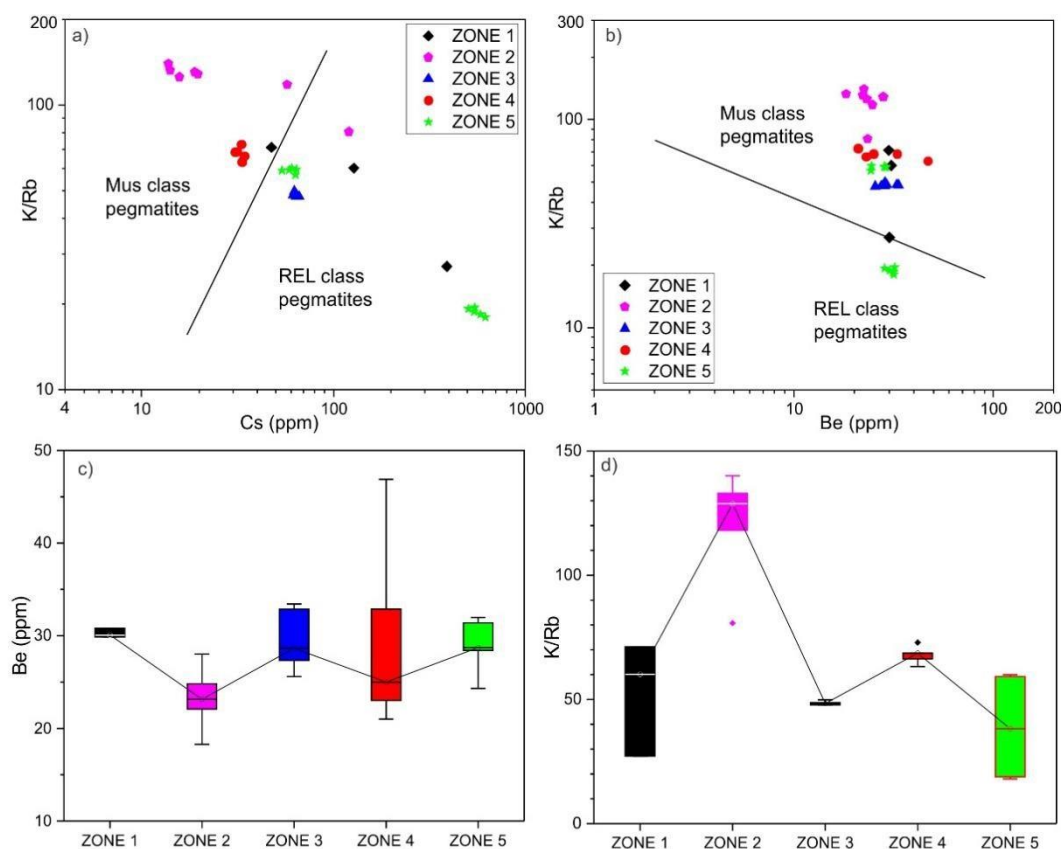
Figure 12. *Cont*.
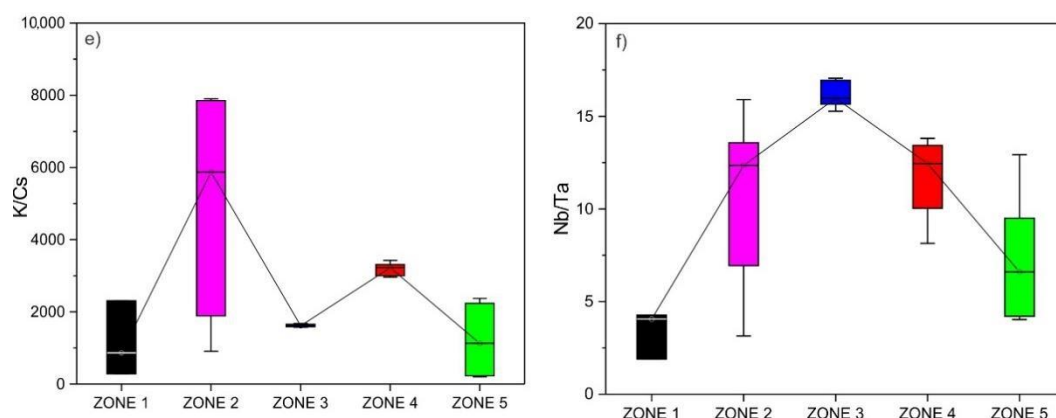
Figure 12. Plots of (**a**) K/Rb vs. Cs (ppm); (**b**) K/Rb vs. Be (ppm); Box and whisker plots of (**c**) Be; (**d**) K/Rb; (**e**) K/Cs; (**f**) Nb/Ta of muscovite from five zones of Yamrang Pegmatite. Connecting lines join the median value. Ratios are calculated from ppm/ppm value. Discrimination lines of Mus-class pegmatites and REL-class pegmatites are from [43], as presented in [40].

6. Discussion

6.1. Classification of the Yamrang Pegmatite

Geoscientists have made many attempts to find a suitable classification scheme for pegmatites [2,3,24,39,44–47]. Ginsburg et al. (1979) [45] divided pegmatites into four categories based on the depth of emplacement, relationship to metamorphism, and granitic plutons: abyssal, muscovite, rare-element (REL) and miarolitic classes. Later this was revised into five classes: abyssal, muscovite, muscovite-rare-element, rare-element, and miarolitic, along with the introduction of two distinct petrogenetic families (LCT and NYF) by Černý and Ercit (2005) [2,3], which are widely used today (Figure 13).
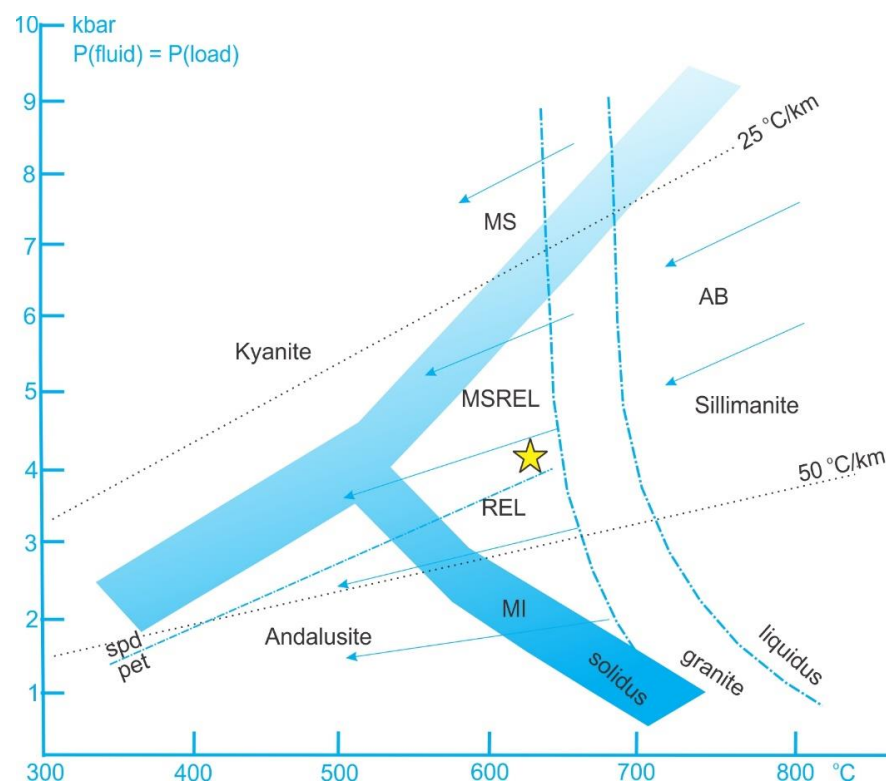
Figure 13. Schematic P-T fields of regional host rocks of five classes of granitic pegmatites: abyssal (AB), muscovite (MS), muscovite - rare-element (MSREL), rare-element (REL), and miarolitic (MI) (redrawn from [3]). Yellow star denotes the Yamrang Pegmatite in the REL pegmatite field.

Economically important, rare-element class pegmatites containing an economic concentration of lithophile rare elements are divided into two subclasses: REL-REE, corresponding to the NYF family, and REL-Li, corresponding to the LCT family. REL-REE subclass pegmatites are derived from post to anorogenic metaluminous to peraluminous granites with allanite, monazite, euxenite, and gadolinite as distinctive minerals. In contrast, REE-Li pegmatites are derived chiefly from syn to late orogenic peraluminous granites and intrude upper-greenschist to amphibolite facies host rocks (Figure 13) with beryl, columbite, tantalite, spodumene, petalite as distinctive minerals [2,3]. The Yamrang Pegmatite intruded into amphibolite facies Ky-Sil grade schistose gneiss, and contains beryl, with columbite-tantalite in inner zones (3–5). These features are consistent with the REL class, beryl type, beryl-columbite subtype pegmatite (Figure 13). The alkali feldspar, having K/Rb 30–150, Rb ~3000 ppm and Cs > 100 ppm, and muscovite having K/Rb 18–50, Rb ~6000 ppm, Cs > 500 ppm and Ta > 65 ppm indicates that the Yamrang Pegmatite is a low to intermediately fractionated REL pegmatite (Figures 10 and 12) [48]. Barton and Young (2002) [49] divided Be-mineralization based on alumina and silica saturation into four types: strongly to weakly peraluminous, metaluminous to weakly peraluminous, peralkaline to metaluminous quartz-saturated, and silica-undersaturated peralkaline types. According to their classification, the pegmatitic Be-mineralization of the Ikhabu pegmatite Field with a high ASI index > 1.2 can be classified as a strong to weak peraluminous type.

Černý (1991) and Černý and Ercit (2005) [2,3] split REL class pegmatites into two distinct petrogenetic families: LCT and NYF types, based on trace element signatures. The LCT family is related to S-type sources in an orogenic setting with a peraluminous nature, abundant rare alkalis, Be, Bo, P and Sn, with a low total REE content (<500 ppm), and a low Nb/Ta ratio. In contrast, the NYF family is related to A-type sources commonly in an anorogenic setting, with a subaluminous to metaluminous nature, enriched HREE and F, and high Nb/Ta ratios [1–3]. The LCT and NYF families were proposed using trace-element signatures expressed by exotic minerals such as spodumene, pollucite, tantalite, pyrochlore, etc., which are only exhibited by the most fractionated pegmatites [2,3,50,51]. Hence, the LCT pegmatites are expected to be enriched in distinctive elements, Li, Cs, and Ta; however, this is not always the case with less fractionated pegmatites. Besides the enrichment of distinctive minerals, several other characteristics are used to classify the pegmatite into the LCT family, such as peraluminous nature, high Be, Rb, Sn, Ga, B, P, F, low total REE content (<500 ppm), low U, Y, Zr, Ti, a mineral assemblage of abundant beryl, tourmaline, muscovite, spessartine, minor presence of topaz, apatite and also association with an orogenic setting [3,50,52,53].

The whole rock geochemistry of the studied pegmatites and granites shows a strong peraluminous nature (ASI index of 1.2–3.3) and plots in the S-type field (Figure 5). The total REE content of the studied pegmatite and granite samples is very low, ranging from 1 to 161 ppm (Supplementary Table S1). The REE chondrite-normalized patterns show a negative slope with a negative Eu anomaly, although some pegmatite samples show a positive Eu anomaly. The primitive mantle normalized multi-element diagrams for the Yamrang Pegmatite show strong enrichment of Cs, Rb, Pb, U, K, and depletion of Ba, Nb, Sr, indicating a continental crustal origin. The Yamrang Pegmatite displays characteristics of low to intermediate fractionation, and does not exhibit an enrichment of distinctive minerals (Li, Cs, Ta) typical of LCT pegmatite; however, its strongly peraluminous nature, low total REE content, mineral assemblage of beryl, tourmaline, spessartine and columbite–tantalite, depletion of Ba and Nb, and enrichment of Pb, Rb and Cs in primitive mantle normalized multi-element plots suggest that the beryl-bearing Yamrang Pegmatite corresponds to the LCT pegmatite family.

This study also shows that the studied orthogneiss and leucogranite are S-type plutons. The S-type source of the orthogneiss and leucogranite agrees with previous research on these Himalaya plutons [54–56]. The S-type leucogranites with Be enrichment (up to 8–11 ppm) support the possibility of rare-metal mineralization prospects in the terrain, as discovered in other parts of the Himalayas [20,57–60].

6.2. Beryl Saturation Process in Yamrang Pegmatite

6.2.1. Magmatic Stage

The rare-element pegmatite whole-rock Be contents are reported in the range of ~32–575 ppm [61,62]. The whole-rock sample from the zone 1 of the Yamrang Pegmatite is enriched in Be (up to 531 ppm; sample YRP-11), but is not beryl saturated with a mineral assemblage of albite (60%), quartz (35%), with subordinate muscovite and tourmaline (5%). The Be content in quartz reported from worldwide REL pegmatites is the lowest (average, 0.1–0.44 ppm) [63,64] of all rock-forming minerals discussed in this paper. Hence, we assigned quartz to the bottom of the Be partition sequence. Albite from zone 1 has a relatively higher calcium component (An_{9-12}) and a higher Be content (~10.4 ppm) than alkali feldspar from other zones (2–4). In addition, the Be content of muscovite (~31 ppm) and tourmaline (~15 ppm) from this zone is relatively higher than from later zones (zones 3, 4) (Be contents of beryl and tourmaline discussed in this paper are taken from our unpublished data). Accordingly, the Be partition sequence as determined by the Be content in coexisting minerals from zone 1 is muscovite > tourmaline > albite > quartz (Figure 14). The Be content in muscovite from zone 2 is (~28 ppm), with tourmaline and perthitic microcline having ~11 ppm and ~7 ppm, respectively. This yields a Be partition sequence of muscovite > tourmaline > microcline > quartz for this zone (Figure 14). Experimental models of beryl saturation show that at high temperatures (~700 °C), 99% of the Be in the melt can be accommodated by rock-forming minerals [65]. While beryl may not crystallize from a melt with 140 ppm Be at 700 °C, at a lower temperature (~400 °C), even 40 ppm Be in the melt can trigger beryl crystallization [65]. Beryl undersaturation in zones 1 and 2 probably occurred due to high-temperature conditions at the early pegmatite intrusion and consolidation stage. Additionally, Be is most compatible in plagioclase with a composition of An_{31}, and Be compatibility decreases with digression from An_{30}, on either side [65]. In agreement with this study, alkali feldspar enriched in the calcic component (An_{9-12}) from marginal zone 1 had a higher Be content (up to 10 ppm) than the inner magmatic zones (zones 2–4). The ASI index of marginal zone 1 is lower (1.7) than that of inner zones (2.2), which may have increased the solubility of Be in the melt, favoring retention in the melt over partitioning into crystals under the higher temperature conditions [66].

Zone 3 is the first zone of magmatic beryl saturation, where beryl coexists with quartz and K-feldspar (microcline). Beryl appears during the late magmatic stages in zone 3 and exhibits a single episode of beryl saturation. This zone has low whole-rock Be content (5–31 ppm), with 4–9 ppm Be in microcline and 4–10 ppm Be in tourmaline, but the zone 3 muscovite has a similar Be content (26–33 ppm) as muscovite in other zones. The Be partition sequence for zone 3 is beryl > muscovite > tourmaline > microcline > quartz (Figure 14). In zone 4, beryl coexists with K-feldspar and quartz at the core margin and forms a beryl and quartz assemblage at the center. The microcline from the zone 4 has the lowest Be content (~4 ppm) among all zones, while muscovite is enriched in Be (21–47 ppm) relative to other zones. It should be noted that microcline and muscovite samples were not precisely taken from the core but were as close to the core as possible. The Be partition sequence for zone 4 is beryl > muscovite > microcline > quartz (Figure 14).

Evensen and London (2002) calculated Be partition coefficients for a variety of rock-forming minerals, demonstrating that Be is compatible in the order of cordierite >> calcic oligoclase (An_{31}) > white mica > dark mica > albite > alkali feldspar $\cong$ quartz [65]. Similarly, Hezel et al. (2011) studied the Be partition sequence among cogenetic minerals in natural samples based on their Be concentration showing the order as staurolite > plagioclase > muscovite > tourmaline > biotite > K-feldspar > garnet [67]. The Be partition sequences among coexisting minerals at the Yamrang Pegmatite magmatic stage is in agreement with these experimental and natural sample data.
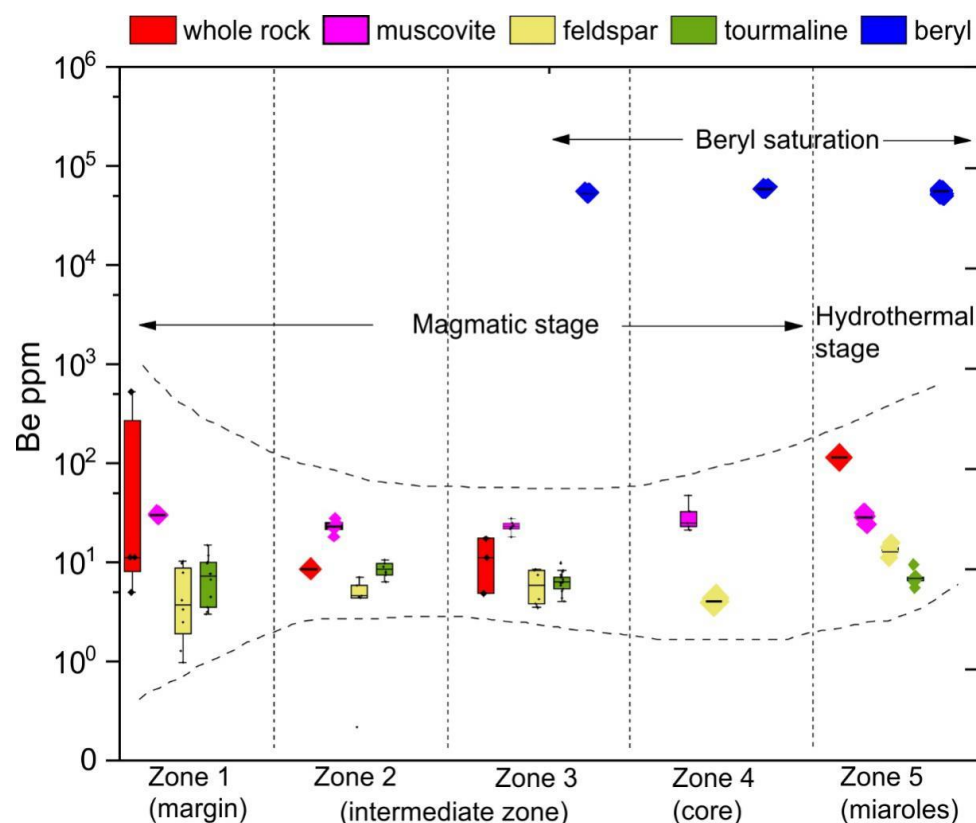
Figure 14. Box and whisker plot of Be-concentration in minerals and whole rock samples from five zones of Yamrang Pegmatite. Zone 1–4 represents the magmatic stage, and zone 5 represents the hydrothermal stage. Beryl saturation occurred at the late magmatic to the hydrothermal stage. Be content of beryl and tourmaline are taken from unpublished data of this author.

Low temperatures were likely prevalent during the late pegmatite crystallization stage, significantly increasing beryl saturation and many other factors likely contributed to beryl saturation in zones 3–5. As crystallization progressed towards the core of the pegmatite, calcic alkali feldspars were deposited in the outer zones, and incompatible elements and fluxes were concentrated in the residual melt. Hence, Be was saturated in the inner zones. In addition, interior zones with a low abundance of minerals compatible with Be, such as calcic albite and tourmaline, may have meant the melt became increasingly enriched in Be, facilitating beryl saturation late in pegmatite crystallization.

6.2.2. Hydrothermal Stage

Miarolitic cavities are empirical evidence of aqueous fluid and record fluid saturation conditions during pegmatite crystallization [50,51,68,69]. Texturally late, miarolitic cavities (designated as zone 5) represent the hydrothermal stage of Yamrang Pegmatite (Figure 14). Zone 5 is not geometrically conformable with previous magmatic zones; rather, it comprises a group of pockets overprinted on magmatic zones along the core margin and along the boundary of zone 2 and 3 in the east portion. Not all pockets have the same mineral assemblages or evolution stages. Beryl-bearing pockets show the highest stage of evolution with a typical mineral assemblage of albite-quartz-muscovite-tourmaline-beryl, which was also obtained experimentally from vapor precipitation [70]. The Be partition sequence among the coexisting minerals from zone 5 is beryl > muscovite > albite > tourmaline > quartz (Figure 14). In contrast to the magmatic zones, we observed Be to be more compatible in albite than in tourmaline in the miarolitic cavities. The pocket-forming *P-T* conditions in the pegmatite system are constrained as 2–3 kbar and 550 °C to as low as 300 °C [45,50,51], suggesting low-temperature conditions during crystallization of zone 5.

Low temperatures can induce beryl saturation at a low concentration of Be in the melt [65]; however, the whole-rock Be content is high (114 ppm) in the miarolitic zone. This suggests Be was enriched in the fluid during the late stages of magmatic crystallization, although Be is less compatible in the vapor phase than in silicate melt with a melt/vapor partition coefficient of 0.2 at 650 °C [70]. A high concentration of Be in the fluid and low-temperature conditions probably facilitated beryl saturation in miarolitic cavities.

6.3. Exploration Implications

Whole rock samples of barren pegmatite yielded < 4.5 ppm of Be, while beryl-pegmatites predominantly had >10 ppm Be (Figure 6), which agrees with the range of Be concentration in fertile granites as listed in [48] (1–604 ppm). The chondrite-normalized REE patterns of beryl-bearing pegmatites have a gentler negative slope than barren pegmatites. The HREE pattern of beryl-pegmatites is flatter than that of barren pegmatites, likely due to the fractionation of garnets. The primitive mantle normalized multi-element diagrams for beryl-pegmatites and barren pegmatites look similar, however, the pattern for beryl pegmatites is steeper with stronger enrichment and depletion of elements, and barren pegmatites show more extreme Ti depletion than beryl pegmatites (Figure 7).

The median K/Rb, K/Cs, and Be content of alkali feldspar and muscovite roughly decreases from outer to inner zones in the Yamrang Pegmatite, reflecting increasing fractionation [2,48,50,71]. However, it should be noted that several fractionation indices break their trend in zone 2 (Figures 10 and 12) and further research will investigate this feature.

The Be content of alkali feldspar ranges from 1 to 16 ppm in the Yamrang Pegmatite. A similar range of alkali feldspar Be content is reported from the Koktokay No. 3 (2–18 ppm) and Luumäki gem beryl pegmatites (7–24 ppm) [72,73]. The median Be content of muscovite shows little variation within zones, ranging from 23 to 30 ppm, similar to the Be concentration range in muscovite from REL-pegmatites such as the Koktokay No. 3 (8–71 ppm), Kenticha (11–38 ppm), and Renli pegmatites (10–23 ppm) [72,74,75]. While the ~10 ppm of Be in alkali feldspar and ~30 ppm of Be muscovite could be a useful indicator of proximal beryl mineralization, the lack of data on Be content in barren pegmatite feldspar and mica make this supposition inconclusive. Nonetheless, whole-rock Be contents of >10 ppm may serve as a potential exploration vector to beryl mineralization in the region. In addition, knowledge of the beryl concentration in zones 3, 4, and 5 may help refine selective mining of the Yamrang Pegmatite.

Beryllium shows a strong positive correlation with Cl, Cr, Ga (r > 0.7) and a strong negative correlation with V, Ni (r < −0.7) in alkali feldspar. These elements in alkali feldspar can also be potential indicators of Be enrichment. We also observed that tourmaline has a significant Be concentration (up to 15 ppm), similar to alkali feldspar (1–16 ppm) in the Yamrang Pegmatite. Tourmaline comprises a significant volume in the marginal zones in pegmatites and likely plays an important role in the Be enrichment process.

Future work should focus on comparing the mineral chemistry of the Yamrang Pegmatite with barren pegmatites and Be-rich leucogranites. More data on mineral geochemistry from different zones will help elucidate Be-enrichment processes during the magmatic and hydrothermal stages.

7. Conclusions

The conclusions of this study can be summarized as follows:

1. The Yamrang Pegmatite can be classified as an intermediate-fractionated REL class, beryl type, beryl-columbite subtype pegmatite of the LCT family.
2. High temperature, low fractionation, dominance of Be-compatible mineral phases such as muscovite, calcium-rich alkali feldspar, and tourmaline resulted in beryl undersaturated marginal zones. In contrast, low temperature, high fractional crystallization, and low abundance of Be-compatible mineral phases resulted in beryl saturated inner zones.

3. The Be partition sequence among coexisting minerals at the magmatic stage is beryl > muscovite > tourmaline > alkali feldspar > quartz, whereas at the hydrothermal stage, the sequence is beryl > muscovite > albite > tourmaline > quartz.

4. A whole rock Be content of >10 ppm may indicate beryl mineralization in the region.

References

1. London, D. A Petrologic Assessment of Internal Zonation in Granitic Pegmatites. *Lithos* **2014**, *184–187*, 74–104. [CrossRef]
2. Černý, P. Rare-Element Granitic Pegmatites. Part I: Anatomy and Internal Evolution of Pegmatite Deposits. *Geosci. Can.* **1991**, *18*, 49–67.
3. Černý, P.; Ercit, T.S. The Classification of Granitic Pegmatites Revisited. *Can. Mineral.* **2005**, *43*, 2005–2026. [CrossRef]
4. Goscombe, B.; Gray, D.; Hand, M. Crustal Architecture of the Himalayan Metamorphic Front in Eastern Nepal. *Gondwana Res.* **2006**, *10*, 232–255. [CrossRef]
5. Imayama, T.; Takeshita, T.; Arita, K. Metamorphic P-T Profile and P-T Path Discontinuity across the Far-Eastern Nepal Himalaya: Investigation of Channel Flow Models. *J. Metamorph. Geol.* **2010**, *28*, 527–549. [CrossRef]
6. Schelling, D. The Tectonostratigraphy and Structure of the Eastern Nepal Himalaya. *Tectonics* **1992**, *11*, 925–943. [CrossRef]
7. Le Fort, P. Himalayas: The Collided Range. Present Knowledge of the Continental Arc. *Am. J. Sci.* **1975**, *275-A*, 1–44.
8. Larson, K.P.; Camacho, A.; Cottle, J.M.; Coutand, I.; Buckingham, H.M.; Ambrose, T.K.; Rai, S.M. Cooling, Exhumation, and Kinematics of the Kanchenjunga Himal, Far East Nepal. *Tectonics* **2017**, *36*, 1037–1052. [CrossRef]
9. Imayama, T.; Takeshita, T.; Yi, K.; Cho, D.-L.; Kitajima, K.; Tsutsumi, Y.; Kayama, M.; Nishido, H.; Okumura, T.; Yagi, K.; et al. Two-Stage Partial Melting and Contrasting Cooling History within the Higher Himalayan Crystalline Sequence in the Far-Eastern Nepal Himalaya. *Lithos* **2012**, *134–135*, 1–22. [CrossRef]
10. Whitney, D.L.; Evans, B.W. Abbreviations for Names of Rock-Forming Minerals. *Am. Mineral.* **2010**, *95*, 185–187. [CrossRef]
11. DeCelles, P.G.; Gehrels, G.E.; Quade, J.; LaReau, B.; Spurlin, M. Tectonic Implications of U-Pb Zircon Ages of the Himalayan Orogenic Belt in Nepal. *Science* **2000**, *288*, 497–499. [CrossRef] [PubMed]
12. Hodges, K.V. Tectonics of the Himalaya and Southern Tibet from Two Perspectives. *GSA Bull.* **2000**, *112*, 324–350. [CrossRef]
13. Parrish, R.R.; Hodges, V. Isotopic Constraints on the Age and Provenance of the Lesser and Greater Himalayan Sequences, Nepalese Himalaya. *Geol. Soc. Am. Bull.* **1996**, *108*, 904–911. [CrossRef]

14. Harrison, M.T.; Grove, M.; Mckeegan, K.D.; Coath, C.D.; Lovera, O.M.; Fort, P.L. Origin and Episodic Emplacement of the Manaslu Intrusive Complex, Central Himalaya. *J. Petrol.* **1999**, *40*, 3–19. [CrossRef]

15. Searle, M.P.; Simpson, R.L.; Law, R.D.; Parrish, R.R.; Waters, D.J. The Structural Geometry, Metamorphic and Magmatic Evolution of the Everest Massif, High Himalaya of Nepal-South Tibet. *J. Geol. Soc. London.* **2003**, *160*, 345–366. [CrossRef]

16. Simpson, R.L.; Parrish, R.R.; Searle, M.P.; Waters, D.J. Two Episodes of Monazite Crystallization during Metamorphism and Crustal Melting in the Everest Region of the Nepalese Himalaya. *Geology* **2000**, *28*, 403. [CrossRef]

17. Searle, M.P.; Szulc, A.G. Channel Flow and Ductile Extrusion of the High Himalayan Slab-the Kangchenjunga-Darjeeling Profile, Sikkim Himalaya. *J. Asian Earth Sci.* **2005**, *25*, 173–185. [CrossRef]

18. Liu, X.C.; Wu, F.Y.; Yu, L.J.; Liu, Z.C.; Ji, W.Q.; Wang, J.G. Emplacement Age of Leucogranite in the Kampa Dome, Southern Tibet. *Tectonophysics* **2016**, *667*, 163–175. [CrossRef]

19. Liu, Z.C.; Wu, F.Y.; Ji, W.Q.; Wang, J.G.; Liu, C.Z. Petrogenesis of the Ramba Leucogranite in the Tethyan Himalaya and Constraints on the Channel Flow Model. *Lithos* **2014**, *208*, 118–136. [CrossRef]

20. Wu, F.; Liu, X.-C.; Liu, Z.-C.; Wang, R.-C.; Xie, L.; Wang, J.; Ji, W.; Yang, L.; Liu, C.; Khanal, G.P.; et al. Highly Fractionated Himalayan Leucogranites and Associated Rare-Metal Mineralization. *Lithos* **2020**, *352–353*, 105319. [CrossRef]

21. Visona, D.; Carosi, R.; Montomoli, C.; Tiepolo, M.; Peruzzo, L. Lithos Miocene Andalusite Leucogranite in Central-East Himalaya (Everest–Masang Kang Area): Low-Pressure Melting during Heating. *Lithos* **2012**, *144–145*, 194–208. [CrossRef]

22. Le Fort, P. Metamorphism and Magmatism during the Himalayan Collision. *Geol. Soc. Lond. Spec. Publ.* **1986**, *19*, 159–172. [CrossRef]

23. Smith, C.P.; Gübelin, E.J.; Bassett, A.M.; Manandhar, M.N. Rubies and Fancy-Color Sapphires from Nepal. *Gems Gemol.* **1997**, *33*, 24–41. [CrossRef]

24. Dill, H.G. Pegmatites and Aplites: Their Genetic and Applied Ore Geology. *Ore Geol. Rev.* **2015**, *69*, 417–561. [CrossRef]

25. ESCAP. *Atlas of Mineral Resources of the ESCAP Region. Geology and Mineral Resources of Nepal. Explanatory Brochure. V. 9*; United Nations: New York, NY, USA, 1993; Volume 9.

26. DMG. *Mineral Resources of Nepal*, 2nd ed.; Department of Mines and Geology: Kathmandu, Nepal, 2017.

27. Li, X.; Liu, Y.; Tu, X.; Hu, G.; Zeng, W. Precise Determination of Chemical Compositions in Silicate Rocks Using ICP-AES and ICP-MS: A Comparative Study of Sample Digestion Techniques of Alkali Fusion and Acid Dissolution. *Geochimica* **2002**, *31*, 289–294. [CrossRef]

28. Monier, G.; Robert, J.L. Muscovite Solid Solutions in the System K_2O-MgO-FeO-Al_2O_3-SiO_2-H_2O: An Experimental Study at 2 Kbar PH_2O and Comparison with Natural Li-Free White Micas. *Mineral. Mag.* **1986**, *50*, 257–266. [CrossRef]

29. Tindle, A.G.; Webb, P.C. Estimation of Lithium Contents in Trioctahedral Micas Using Microprobe Data: Application to Micas from Granitic Rocks. *Eur. J. Mineral.* **1990**, *2*, 595–610. [CrossRef]

30. Xie, L.; Zhang, Y.; Zhang, H.; Sun, J.; Wu, F. In Situ Simultaneous Determination of Trace Elements, U-Pb and Lu-Hf Isotopes in Zircon and Baddeleyite. *Chin. Sci. Bull.* **2008**, *53*, 1565–1573. [CrossRef]

31. Wu, S.; Karius, V.; Schmidt, B.C.; Simon, K.; Wörner, G. Comparison of Ultrafine Powder Pellet and Flux-Free Fusion Glass for Bulk Analysis of Granitoids by Laser Ablation-Inductively Coupled Plasma-Mass Spectrometry. *Geostand. Geoanalytical Res.* **2018**, *42*, 575–591. [CrossRef]

32. Wu, S.; Wörner, G.; Jochum, K.P.; Stoll, B.; Simon, K.; Kronz, A. The Preparation and Preliminary Characterisation of Three Synthetic Andesite Reference Glass Materials (ARM-1, ARM-2, ARM-3) for In Situ Microanalysis. *Geostand. Geoanalytical Res.* **2019**, *43*, 567–584. [CrossRef]

33. Griffin, W.L. GLITTER: Data Reduction Software for Laser Ablation ICP-MS. *Laser Ablation ICP-MS Earth Sci. Curr. Pract. Outst. Issues* **2008**, 308–311.

34. Rushmer, T.; Knesel, K. Defining Geochemical Signatures and Timescales of Melting Processes in the Crust: An Experimental Tale of Melt Segregation, Migration and Emplacement. In *Timescales of Magmatic Processes*; John Wiley & Sons, Ltd.: Chichester, UK, 2010; pp. 181–211. [CrossRef]

35. Middlemost, E.A.K. Naming Materials in the Magma/Igneous Rock System. *Earth-Sci. Rev.* **1994**, *37*, 215–224. [CrossRef]

36. Maniar, P.D.; Piccoli, P.M. Tectonic Discrimination of Granitoids. *GSA Bull.* **1989**, *101*, 635–643. [CrossRef]

37. Boynton, W.V. Cosmochemistry of the Rare Earth Elements: Meteorite Studies. *Dev. Geochem.* **1984**, *2*, 63–114. [CrossRef]

38. Sun, S.-S.; McDonough, W.F. Chemical and Isotopic Systematics of Oceanic Basalts: Implications for Mantle Composition and Processes. *Geol. Soc. Lond. Spec. Publ.* **1989**, *42*, 313–345. [CrossRef]

39. Trueman, D.L.; Černý, P. Exploration for Rare-Element Granitic Pegmatites. In Proceedings of the Short Course in Granitic Pegmatites in Science and Industry; Mineralogical Association of Canada: Quebec, QC, Canada, 1982; pp. 463–493.

40. Morteani, G.; Preinfalk, C.; Horn, A.H. Classification and Mineralization Potential of the Pegmatites of the Eastern Brazilian Pegmatite Province. *Miner. Depos.* **2000**, *35*, 638–655. [CrossRef]

41. Tischendorf, G.; Gottesmann, B.; Förster, H.-J.; Trumbull, R.B. On Li-Bearing Micas: Estimating Li from Electron Microprobe Analyses and an Improved Diagram for Graphical Representation. *Mineral. Mag.* **1997**, *61*, 809–834. [CrossRef]

42. Miller, C.F.; Stoddard, E.F.; Bradfish, L.J.; Dollase, W.A. Composition of Plutonic Muscovite: Genetic Implications. *Can. Mineral.* **1981**, *19*, 25–34.

43. Cerny, P.; Burt, D.M. Paragenesis, Crystallochemical Characteristics, and Geochemical Evolution of the Micas in Granite Pegmatites. *Rev. Mineral. Geochem.* **1984**, *13*, 257–297.

44. Cameron, E.N.; Jahns, R.H.; Mcnair, A.H.; Page, L.R. Internal Structure of Granitic Pegmatites, No. 2. *Econ. Geol. Urbana. Ill.* **1949**, *2*, 115.

45. Ginsburg, A.I.; Timofeyev, I.N.; Feldman, L.G. Principles of Geology of the Granitic Pegmatites. *Nedra. Moscow* **1979**, 296.

46. Zagorsky, V.Y.; Makagon, V.M.; Shmakin, B.M. The Systematics of Granitic Pegmatites. *Can. Mineral.* **1999**, *37*, 800–802.

47. Černý, P. Anatomy and Classification of Granitic Pegmatites. In *Granitic Pegmatites in Science and Industry*; Černý, P., Ed.; Mineralogical Association of Canada: Québec, QC, Canada, 1982; Volume 8, pp. 1–39.

48. Selway, J.B.; Breaks, F.W.; Tindle, A.G. A Review of Rare-Element (Li-Cs-Ta) Pegmatite Exploration Techniques for the Superior Province, Canada, and Large Worldwide Tantalum Deposits. *Explor. Min. Geol.* **2005**, *14*, 1–30. [CrossRef]

49. Barton, M.D.; Young, S. Non-Pegmatitic Deposits of Beryllium: Mineralogy, Geology, Phase Equilibria and Origin. *Rev. Mineral. Geochem.* **2002**, *50*, 591–691. [CrossRef]

50. London, D. *Pegmatites*; Martin, R.F., Ed.; Mineralogical Association of Canada: Quebec, QC, Canada, 2008; Volume 10.

51. London, D. Ore-Forming Processes within Granitic Pegmatites. *Ore Geol. Rev.* **2018**, *101*, 349–383. [CrossRef]

52. Černý, P.; London, D.; Novák, M. Granitic Pegmatites as Reflections of Their Sources. *Elements* **2012**, *8*, 289–294. [CrossRef]

53. Duc-Tin, Q.; Keppler, H. Monazite and Xenotime Solubility in Granitic Melts and the Origin of the Lanthanide Tetrad Effect. *Contrib. Mineral. Petrol.* **2015**, *169*, 1–26. [CrossRef]

54. Gehrels, G.E.; DeCelles, P.G.; Martin, A.; Ojha, T.P.; Pinhassi, G.; Upreti, B.N. Initiation of the Himalayan Orogen as an Early Paleozoic Thin-Skinned Thrust Belt. *GSA Today* **2003**, *13*, 4. [CrossRef]

55. Cawood, P.A.; Johnson, M.R.W.; Nemchin, A.A. Early Palaeozoic Orogenesis along the Indian Margin of Gondwana: Tectonic Response to Gondwana Assembly. *Earth Planet. Sci. Lett.* **2007**, *255*, 70–84. [CrossRef]

56. Hopkinson, T.N.; Harris, N.B.W.; Warren, C.J.; Spencer, C.J.; Roberts, N.M.W.; Horstwood, M.S.A.; Parrish, R.R.; EIMF. The Identification and Significance of Pure Sediment-Derived Granites. *Earth Planet. Sci. Lett.* **2017**, *467*, 57–63. [CrossRef]

57. Wang, J.-G.; Liu, X.-C.; Liu, Z.-C.; Ji, W.-Q.; Wu, F.-Y.; Ding, L. Highly Fractionated Late Eocene (~35 Ma) Leucogranite in the Xiaru Dome, Tethyan Himalaya, South Tibet. *Lithos* **2015**, *240–243*, 337–354. [CrossRef]

58. Liu, C.; Wang, R.-C.; Wu, F.-Y.; Xie, L.; Liu, X.-C.; Li, X.-K.; Yang, L.; Li, X.-J. Spodumene Pegmatites from the Pusila Pluton in the Higher Himalaya, South Tibet: Lithium Mineralization in a Highly Fractionated Leucogranite Batholith. *Lithos* **2020**, *358–359*, 105421. [CrossRef]

59. Qin, K.; Zhao, J.; He, C.; Shi, R. Discovery of the Qongjiagang Giant Lithium Pegmatite Deposit in Himalaya, Tibet, China. *Acta Petrol. Sin.* **2021**, *37*, 3277–3286. [CrossRef]

60. Zhou, Q.; Qin, K.; He, C.; Wu, H.; Liu, Y.; Niu, X.; Mo, L.; Liu, X.; Zhao, J. Li-Be-Nb-Ta Mineralogy of the Kuqu Leucogranite and Pegmatite in the Eastern Himalaya, Tibet, and Its Implication. *Acta Petrol. Sin.* **2021**, *37*, 3305–3324. [CrossRef]

61. London, D.; Evensen, J.M. Beryllium in Silicic Magmas and the Origin of Beryl-Bearing Pegmatites. *Rev. Mineral. Geochem.* **2002**, *50*, 445–486. [CrossRef]

62. Zhao, J.; He, C.; Qin, K.; Shi, R.; Liu, X.; Hu, F.; Yu, K.; Sun, Z. Geochronology, Source Features and the Characteristics of Fractional Crystallization in Pegmatite at the Qongjiagang Giant Pegmatite-Type Lithium Deposit, Himalaya, Tibet. *Acta Petrol. Sin.* **2021**, *37*, 3325–3347. [CrossRef]

63. Müller, A.; Keyser, W.; Simmons, W.B.; Webber, K.; Wise, M.; Beurlen, H.; Garate-Olave, I.; Roda-Robles, E.; Galliski, M.Á. Quartz Chemistry of Granitic Pegmatites: Implications for Classification, Genesis and Exploration. *Chem. Geol.* **2021**, *584*, 120507. [CrossRef]

64. Breiter, K.; Ďurišová, J.; Dosbaba, M. Chemical Signature of Quartz from S- and A-Type Rare-Metal Granites – A Summary. *Ore Geol. Rev.* **2020**, *125*, 103674. [CrossRef]

65. Evensen, J.M.; London, D. Experimental Silicate Mineral/Melt Partition Coefficients for Beryllium and the Crustal Be Cycle from Migmatite to Pegmatite. *Geochim. Cosmochim. Acta* **2002**, *66*, 2239–2265. [CrossRef]

66. Evensen, J.M.; London, D.; Wendlandt, R.F. Solubility and Stability of Beryl in Granitic Melts. *Am. Mineral.* **1999**, *84*, 733–745. [CrossRef]

67. Hezel, D.C.; Angelika, K.; Marschall, H.R.; Ludwig, T.; Meyer, H.P. Major-Element and Li, Be Compositional Evolution of Tourmaline in an S-Type Granite-Pegmatite System and Its Country Rocks: An Example from Ikaria, Aegean Sea, Greece. *Can. Mineral.* **2011**, *49*, 321–340. [CrossRef]

68. Simmons, W.B.; Pezzotta, F.; Shigley, J.E.; Beurlen, H. Granitic Pegmatites as Sources of Colored Gemstones. *Elements* **2012**, *8*, 281–287. [CrossRef]

69. Jahns, R.H.; Burnham, C.W. Experimental Studies of Pegmatite Genesis; l, A Model for the Derivation and Crystallization of Granitic Pegmatites. *Econ. Geol.* **1969**, *64*, 843–864. [CrossRef]

70. London, D.; Hervig, R.L.; Morgan, G.B. Melt-Vapor Solubilities and Elemental Partitioning in Peraluminous Granite-Pegmatite Systems: Experimental Results with Macusani Glass at 200 MPa. *Contrib. Mineral. Petrol.* **1988**, *99*, 360–373. [CrossRef]

71. Cerny, P.; Meintzer, R.E.; Anderson, A.J. Extreme Fractionation in Rare-Element Granitic Pegmatites: Selected Examples of Data and Mechanisms. *Can. Mineralogist.* **1985**, *23*, 381–421.

72. Zhou, Q.; Qin, K.; Tang, D.; Ding, J.; Guo, Z. Mineralogy and Significance of Micas and Feldspars from the Koktokay No. 3 Pegmatitic Rare-Element Deposit, Altai. *Acta Petrol. Sin.* **2013**, *29*, 3004–3022.

73. Michallik, R.M.; Wagner, T.; Fusswinkel, T.; Heinonen, J.S.; Heikkilä, P. Chemical Evolution and Origin of the Luumäki Gem Beryl Pegmatite: Constraints from Mineral Trace Element Chemistry and Fractionation Modeling. *Lithos* **2017**, *274–275*, 147–168. [CrossRef]

74. Küster, D.; Romer, R.L.; Tolessa, D.; Zerihun, D.; Bheemalingeswara, K.; Melcher, F.; Oberthür, T. The Kenticha Rare-Element Pegmatite, Ethiopia: Internal Differentiation, U–Pb Age and Ta Mineralization. *Miner. Depos.* **2009**, *44*, 723–750. [CrossRef]

75. Li, P.; Li, J.; Chen, Z.; Liu, X.; Huang, Z.; Zhou, F. Compositional Evolution of the Muscovite of Renli Pegmatite-Type Rare-Metal Deposit, Northeast Hunan, China: Implications for Its Petrogenesis and Mineralization Potential. *Ore Geol. Rev.* **2021**, *138*, 104380. [CrossRef]